

This document is confidential and is proprietary to the American Chemical Society and its authors. Do not copy or disclose without written permission. If you have received this item in error, notify the sender and delete all copies.

De novo design of functional co-assembling organic-inorganic hydrogels for hierarchical mineralization and neovascularization

Journal:	ACS Nano
Manuscript ID	nn-2020-098149.R1
Manuscript Type:	Article
Date Submitted by the Author:	n/a
Complete List of Authors:	Okesola, Babatunde; Queen Mary University of London, Institute of Bioengineering, School of Engineering and materials Science Mendoza-Martinez, Ana; Queen Mary University of London, Institute of Bioengineering, School of Engineering and Materials Science Cidonio, Gianluca; University of Southampton, Bone and Joint Research Group, Centre for Human Development, Stem Cells and Regeneration, Institute of Developmental Sciences Derkus, Burak; Eskisehir Osmangazi University, Biomedical Engineering Boccorh, Delali; University of Strathclyde, Pure and Applied Chemistry Osuna de la Peña, David; Queen Mary University of London, Institute of Bioengineering, School of Engineering and materials Science Elsharkawy, Sherif; King's College London, Centre for Oral, Clinical, and Translational Sciences, Faculty of Dentistry, Oral, and Craniofacial Sciences Wu, Yuanhao; University of Nottingham, School of Pharmacy, Biodiscovery Institute Dawson, Jonathan; University of Southampton, Faculty of Medicine Wark, Alastair; University of Strathclyde, Chemistry Knani, Dafna; Braude College, Biotechnology engineering Adams, Dave; University of Glasgow, School of Chemistry Oreffo, Richard; University of Southampton, Institute of Developmental Sciences Mata, Alvaro ; University of Nottingham,

SCHOLARONE™
Manuscripts

De novo design of functional co-assembling organic-inorganic hydrogels for hierarchical mineralization and neovascularization

Babatunde O. Okesola^{1,2}, Ana Karen Mendoza-Martinez^{1,2}, Gianluca Cidonio³, Burak Derkus^{1,2,4}, Delali K. Boccorh⁵, David Osuna de la Peña², Sherif Elsharkawy⁶, Yuanhao Wu^{7,8}, Jonathan I. Dawson³, Alastair W. Wark⁵, Dafna Knani⁹, Dave J. Adams¹⁰, Richard O. C. Oreffo³, Alvaro Mata^{1,2,7,8,11*}

1. Institute of Bioengineering, Queen Mary University of London, London, E1 4NS, UK.
2. School of Engineering and Materials Science, Queen Mary University of London, London, E1 4NS, UK.
3. Bone and Joint Research Group, Centre for Human Development, Stem Cells and Regeneration, Institute of Developmental Sciences, University of Southampton, Southampton, SO16 6YD, UK.
4. Department of Chemistry, Faculty of Science, Ankara University, 06560 Ankara, Turkey.
5. Centre for Molecular Nanometrology, Department of Pure and Applied Chemistry, Technology and Innovation Centre, University of Strathclyde, Glasgow, G1 1RD, UK.
6. Centre for Oral, Clinical, and Translational Sciences, Faculty of Dentistry, Oral, and Craniofacial Sciences, King's College London, London, SE1 9RT, UK.
7. School of Pharmacy, University of Nottingham, Nottingham, NG7 2RD, UK.
8. Biodiscovery Institute, University of Nottingham, Nottingham, NG7 2RD, UK.
9. Department of Biotechnology Engineering, ORT Braude College, Karmiel 2161002, Israel.
10. School of Chemistry, College of Science and Engineering, University of Glasgow, Glasgow, G12 8QQ, UK.
11. Department of Chemical and Environmental Engineering, University of Nottingham, Nottingham, NG7 2RD, UK.

Corresponding author: a.mata@nottingham.ac.uk

Abstract

Synthetic nanostructured materials incorporating both organic and inorganic components offer a unique, powerful and versatile class of materials for widespread applications due to the distinct, yet complementary, nature of the intrinsic properties of the different constituents. We report a supramolecular system based on synthetic nanoclay (Laponite™, **Lap**) and peptide amphiphiles (PAs, **PAH3**) rationally designed to co-assemble into nanostructured hydrogels with high structural integrity and a spectrum of bioactivities. Spectroscopic and scattering techniques and molecular dynamic simulation approaches were harnessed to confirm that **PAH3** nanofibers electrostatically adsorbed and conformed to the surface of **Lap** nanodisks. Electron and atomic force microscopies also confirmed an increase in diameter and surface area of **PAH3** nanofibers after co-assembly with **Lap**. Dynamic oscillatory rheology revealed that the co-assembled **PAH3-Lap** hydrogels displayed high stiffness and robust self-healing behaviour while gas adsorption analysis confirmed a hierarchical and heterogeneous porosity. Furthermore, this distinctive structure within the three-dimensional matrix (3D) provided spatial confinement for the nucleation and hierarchical organization of high-aspect ratio hydroxyapatite nanorods into well-defined spherical clusters within the 3D matrix. Applicability of the organic-inorganic **PAH3-Lap** hydrogels was assessed *in vitro* using human bone marrow-derived stromal cells (hBMSCs) and *ex vivo* using a chick chorioallantoic membrane (CAM) assay. The results demonstrated that the organic-inorganic **PAH3-Lap** hydrogels promote human skeletal cell proliferation and, upon mineralization, integrate with the CAM, are infiltrated by blood vessels, stimulate extracellular matrix production, and facilitate extensive mineral deposition relative to the controls.

KEYWORDS: Laponite™, nanocomposite hydrogels, co-assembly, supramolecular, biomineralization, peptide amphiphiles, multicomponent biomaterials

1. Introduction

Nature contains an array of functional nanomaterials that result from the supramolecular co-assembly of organic and inorganic building blocks across multiple length scales. Materials such as tooth enamel, bones, nacre from mollusc shells, and marine diatom frustules exhibit a high level of precision over their molecular composition, hierarchical structure, and morphology. The inherent characteristics endows these nanomaterials with remarkable properties ranging from high stiffness to light-emission.^{1, 2} A fundamental characteristic of natural organic-inorganic composites is the presence of organic matrixes exhibiting ordered arrays of confined charged groups, which induce and regulate the spatial nucleation and hierarchical organization of crystals.^{3, 4} These organic components are generally 3D hydrogel-like materials made from multiple components such as proteins, peptides, polyamines, and polysaccharides.^{5, 6}

This bottom-up “nanofabrication” strategy employed by nature, has been harnessed in materials science to design organic-inorganic multicomponent hydrogels with innovative properties.^{2, 7} In particular, significant research efforts have been expended to integrate the intrinsic electrical conductivity, magnetism, adhesiveness, and hardness of inorganic nanomaterials⁸ with the inherent functionality of both natural (*e.g.* collagen,⁹ elastin,¹⁰ DNA,¹¹ and hyaluronic acid¹²) and synthetic (*e.g.* dibenzylidene-d-sorbitol,^{8, 13} peptides,⁷ and polymers¹⁴) molecules in the design of advanced organic-inorganic hydrogels. These organic-inorganic multicomponent hydrogels are attractive platforms for a wide range of applications in optics, micro-electronics, energy storage, catalysis, sensing/environmental clean-up, and nanomedicine.¹⁵ However, the resulting structures and functions exhibited by these composite materials remain far from those of the natural organic-inorganic materials.¹⁶

To enhance the properties of organic-inorganic nanocomposites, co-organization of two or more types of inorganic components within the same nanoscale object, provides an opportunity to prepare higher-ordered nano-objects with synergistic properties.¹⁷ Thus, application of such an inorganics approach, takes advantage of the distinct properties of the individual inorganics as well as emergence of new ones that result from their interactions. Current strategies for fabricating organic-inorganic nanocomposites with multi-inorganic nano-objects are driven by either programmed assembly or, reaction-diffusion mechanisms. Programmed assembly involves

molecular recognition-driven interparticle aggregation. For example, in a seminal work by Mann and co-workers, DNA-directed attachment of gold nanoparticles to single nanoparticles of silica was used to fabricate discrete nano-objects.¹⁸ Similarly, barstar-capped iron oxide nanoparticles and barnase-coated quantum dot nanoparticles were co-assembled to create superstructures with magneto-fluorescence properties.¹⁹ Other approaches using complementary streptavidin/biotin or antibody/antigen have been harnessed to integrate multiple inorganics in a single organic-inorganic nanocomposite.²⁰ In contrast, systems based on reaction-diffusion mechanisms enable assembly of inorganics into nano-objects with spatio-temporal orientation, not readily accessible by equilibrium processes.^{17,19} Examples have been demonstrated in biomineralization,²¹ microfabrication,²²⁻²⁷ formation of microlenses,²⁸ and dynamic materials.²⁹ Reactions of inorganic species, coupled with diffusion in hydrogel media can lead to the formation of nano-objects with structural hierarchy and complexity as well as multifunctional properties. The rate of formation of these nano-objects within a hydrogel can be controlled by fluid flow, spontaneous compartmentalization, diffusive transport, and Ostwald ripening.³⁰

Self-assembling peptides are particularly attractive platforms for the design of organic-inorganic nanostructures, given their intrinsic propensity to assemble into 3D hydrogels, comprising well-defined nanostructures and an ability to display tunable binding affinity for inorganic nanostructures.³¹ These unique attributes of self-assembling peptides, have been harnessed to fabricate diverse peptide-inorganic hybrid materials with impressive properties and functionalities. The ability to harness the spatio-temporal organisation and enhanced surface chemistry of peptide-inorganic hydrogels would represent a step-change platform to guide crystal morphogenesis in 3D confinement.⁷

Laponite™ XLG (Lap), a trioctahedral synthetic hectorite ($\text{Na}^{+0.7}[(\text{Si}_8\text{Mg}_{5.5}\text{Li}_{0.3})\text{O}_{20}(\text{OH})_4]^{-0.7}$), is a particularly important class of nanosilicate being explored for the design of functional nanomaterials.³² Lap displays an ultrathin 2D nanostructure (diameter = 25 – 30 nm and thickness < 1 nm), discotic charged surface (permanent negative charge on the surface and positive rim charge), high specific surface area ($800 \text{ m}^2/\text{g}$), and optical transparency.³³ Consequently, Lap has been co-assembled with synthetic polymers,³⁴⁻³⁶ DNA,³⁷ or proteins^{9, 38} to develop organic-inorganic hydrogels for numerous biomedical applications and additive manufacturing.³² For

example, there is a growing interest in the use of polymer-Laponite nanocomposite hydrogels as injectable vehicles for biological cargo including cells,³⁹ drug molecules,⁴⁰ and growth factors⁴¹, because of their intrinsic shear-thinning property. However, synthetic polymers typically require complex chemical synthesis and purification steps and lack a well-defined structure-property relationship, while natural polymers lack structural tunability and can be difficult to obtain. Therefore, the use of modular and easy-to-synthesize organic building blocks such as self-assembling peptides, can serve as simpler and more predictable components to interact with and guide the assembly of Lap. Peptide amphiphiles (PAs), a class of self-assembling peptides, have been engineered to facilitate co-assembly with biomolecules such as hyaluronic acid,⁴² elastin-like polypeptides,⁴³ keratin,⁴⁴ resilin-like polypeptide⁴⁵ as well as non-peptidic molecules⁴⁶ to generate different architectures with structural hierarchy and enhanced mechanical and functional properties.

Herein, we report an organic-inorganic nanocomposite hydrogel based on the co-assembly of Lap nanodisks with PAs. The hydrogels displayed high mechanical strength, shear-thinning behaviour, and molecular diversity. Furthermore, the resulting PA-Lap co-assembled structures served as spatial confinements to guide the formation of nanocrystals with well-defined morphologies across multiple length scales, leading to the formation of multi-inorganic-organic nano-objects (schematically illustrated in Fig. 1). These mineralized hydrogels supported cell adhesion, proliferation, differentiation, and neovascularization as assessed by *in vitro* cell culture and *ex vivo* using a chick chorioallantoic membrane (CAM) assay.

2. Results and discussion

Rationale of the material design

Our system aims to harness the intrinsic discotic and surface anisotropy of Lap nanodisks and the modularity and self-assembling capacity of PAs to engineer robust and biocompatible hydrogels that not only exhibit the properties of each component but, critically, new emergent properties as a result of their co-assembly. The PA (**PAH3**) is a histidine-rich molecule ($\text{CH}_3\text{-(CH}_2\text{)}_{14}\text{-CONH-VVVAHHH-CONH}_2$, Fig. 1g) is designed to co-assemble through interaction with **Lap**. The unique aromatic imidazole side chain of histidine is key to the self-assembly of proteinaceous

fibers driven by organic-inorganic complexation, which is known to generate self-healable and mechanically reinforced biogenic architectures.⁴⁷ We reasoned that the histidine aromatic imidazole side chain ($pK_a \sim 6.0$), which becomes cationic in mildly acidic conditions, would promote electrostatic and intercalation interactions between **PAH3** and the negatively charged **Lap** disk surfaces (surface adsorption). Based on the pioneering work of Aida and co-workers on co-assembling Lap nanodisks with guanidinium-based dendritic binders⁴⁸, we hypothesized that our **PAH3-Lap** co-assembling system would generate mechanically reinforced organic-inorganic hydrogels. It is noteworthy that although cationic PAs with lysine charged head groups have been extensively exploited, self-assembly and gelation of histidine-based **PAH3** have yet to be explored. **PAK3** ($\text{CH}_3-(\text{CH}_2)_{14}-\text{CONH-VVVAACKKK}-\text{CONH}_2$) and **PAE3** ($\text{CH}_3-(\text{CH}_2)_{14}-\text{CONH-VVVAEEEE}-\text{CONH}_2$) were used as controls throughout the experiments.

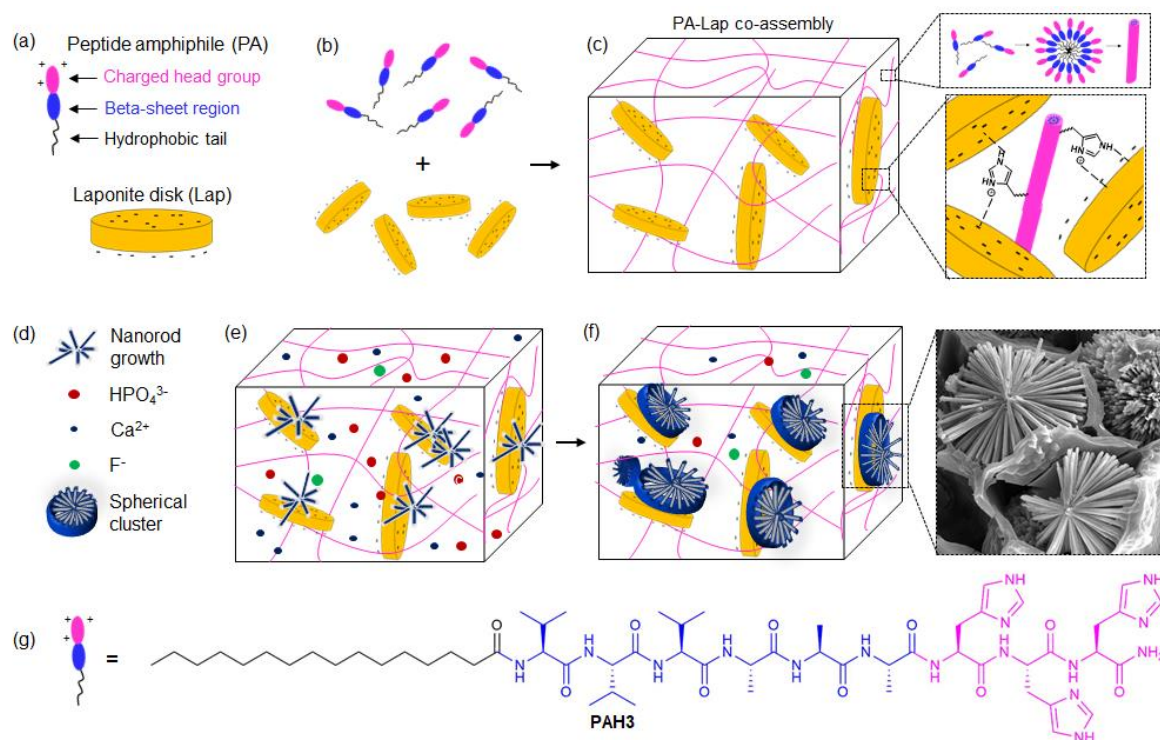


Figure 1. Supramolecular co-assembly of exfoliated Lap nanodisks (-ve) and PA (+ve) to create 3D hydrogels able to guide nucleation and hierarchical growth of hydroxyapatite crystals. (a) Structural representation of a peptide amphiphile (PA) with its domains and a Lap nanodisk. (b) Supramolecular co-assembly of PAs and Lap to create (c) mechanically robust organic-inorganic hybrid hydrogels with interconnected nanofibers physically cross-linked by Lap nanodisks. Diffusion of (d) mineralizing ionic species into the 3D organic-inorganic hybrid hydrogels triggers the (e) nucleation and (f) hierarchical crystal growth of hydroxyapatite crystals into high aspect ratio nanorods organized in spherical clusters. (g) Structural formula for histidine-based PAs.

176 Mechanism of PAH3-Lap supramolecular co-assembly

177 *Electrostatic and sergeant-soldier interactions drive co-assembly*

178 PAs were designed and synthesized as previously reported.⁴⁹ To assess electrostatic interactions
179 between **PAH3** and **Lap** nanodisks, we measured the zeta potential (ζ) values and hydrodynamic
180 radii (R_h) of individual components against their mixture. The interaction between **Lap** ($\zeta = -35$
181 mV, $R_h = 36.42 \pm 2.01$ nm) and **PAH3** ($\zeta = +25$ mV, $R_h = 80.11 \pm 4.31$ nm) evidently revealed
182 the formation of a higher-ordered nanostructure with an increased hydrodynamic radius ($\zeta = -10$
183 mV, $R_h = 115.11 \pm 6.54$ nm) (Supplementary Figure S1a-e). In contrast, the control **PAE3** (-30
184 mV), which exhibits similar net charge as **Lap**, did not display any interaction, suggesting that the
185 formation of **PAH3-Lap** was at least partly driven by electrostatic interactions.

186
187 Given that PAs are generally known to self-assemble into β -sheets, we used circular dichroism
188 (CD) spectroscopy to assess interaction between **PAH3** and **Lap** nanodisks. The CD
189 measurements revealed that **PAH3** displays a typical β -sheet conformation with an absorption
190 maxima and minima at 202 and 218 nm, respectively (Fig. 2a). Upon co-assembly with **Lap**, the
191 CD intensities at 202 and 218 nm decreased by ~ 16 and ~ 11 mdeg, respectively. This significant
192 decrease in CD intensities might be due to strong surface adhesion of **PAH3** to the **Lap** nanodisks,
193 resulting in a significant disruption of the **PAH3** β -sheet conformation. Such disruption has been
194 previously reported in silk molecules upon interaction with Lap.³⁷ To further confirm surface
195 adsorption of **PAH3** to **Lap**, we used a standard molecular probe thioflavin T (ThT) which is
196 known to monitor PA self-assembly in aqueous environments.⁴⁶ When the achiral ThT was
197 introduced into a diluted **PAH3-Lap** hydrogel, a negative band at 410 nm, which is indicative of
198 bound ThT, became apparent (Fig. 2b). This absorption band was not observed when ThT was
199 mixed with **PAH3** in water, **PAH3** in PBS, or **Lap** in water. Although ThT co-assembled with the
200 **Lap** nanodisk suspension, the Lap-ThT complex exhibited no CD signal, suggesting that ThT
201 acquired an induced chirality due to surface adsorption to Lap nanodisks templated by **PAH3**
202 nanofibers (Fig. 2b inset). Such nanofiber templating of **Lap** nanodisks has been previously
203 demonstrated with collagen nanofibers due to electrostatic interactions between the positively
204 charged amino acid groups on the periphery of the collagen nanofibrils and negatively charged
205 **Lap** surfaces.⁵⁰

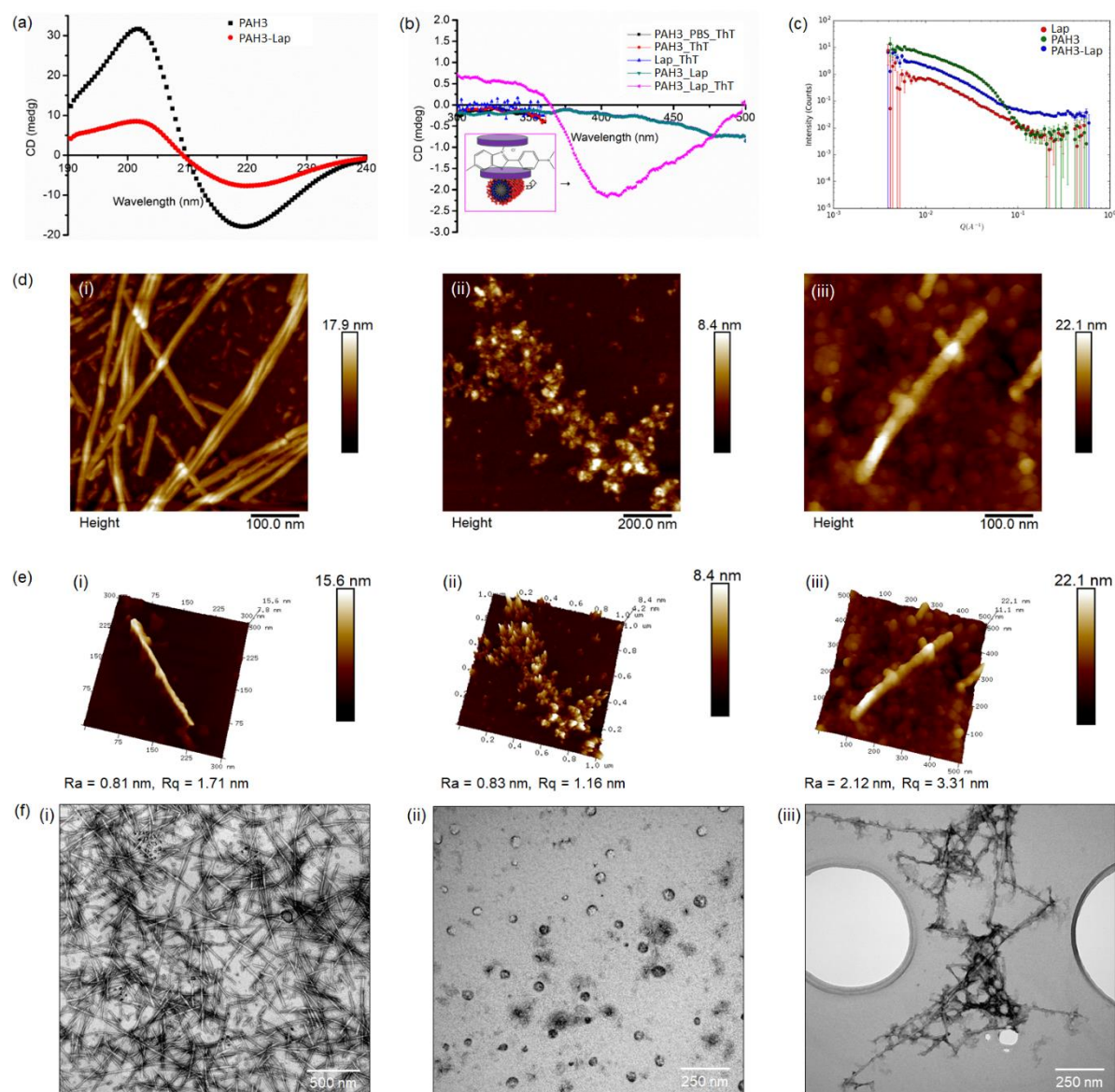


Figure 2. Structural characterisation of supramolecular co-assembly. (a) CD spectra of an aqueous solution of PAH3 before (square traces) and after adding Lap (circular traces). (b) Induced CD spectra of thioflavin T (ThT) in the presence of **PAH3** in PBS 1x, **PAH3-Lap** partial hydrogels, and aqueous solution of **Lap**. Inset represent proposed mechanism for chirality transfer from **PAH3** to **Lap** nanodisk as a result of supramolecular co-assembly, which was confirmed with the use of the molecular rotor ThT. (c) Synchrotron small-angle neutron scattering of **PAH3**, **Lap**, and **PAH3-Lap** co-assembly. (d) Atomic force micrographs of (i) **PAH3**, (ii) **Lap**, and (iii) **PAH3-Lap** co-assembly as well as the (e) surface topography profile for (i) **PAH3**, (ii) **Lap**, and (iii) **PAH3-Lap** co-assembly. (f) Transmission electron micrographs of aqueous suspension of (i) **PAH3**, (ii) **Lap**, and (iii) **PAH3-Lap**.

220 *Nanoscopic evidence of PA-Lap co-assembly*

221 Nanoscale characterization of the **PAH3-Lap** composites also confirmed supramolecular
222 integration of both components to generate a higher-ordered nanostructure. First, we used
223 synchrotron small-angle neutron scattering (SANS) to characterize the individual components
224 (**Lap** and **PAH3**), as well as their mixture (**PAH3-Lap**). The SANS data for **Lap** alone in
225 deuterium oxide (D₂O) possesses a $Q^{-1.8}$ dependency in the range $0.01 < Q < 0.1 \text{ \AA}^{-1}$, which is
226 consistent with a thin disk-shaped structure with a thickness and diameter of ~ 12 and $\sim 256 \text{ \AA}$,
227 respectively (Fig. 2c, Supplementary Table S1). The SANS data for **PAH3** alone in D₂O shows
228 the existence of a cylinder-like nanostructures with a radius of $\sim 38 \text{ \AA}$ and several microns in
229 length. The scattering profile of the mixture of **Lap** and **PAH3** shows co-existence of both disk-
230 like nanostructures and cylindrical nanofibers, suggesting a supramolecular co-assembly of both
231 nanostructures. The radius of **PAH3** nanofibers increased by $\sim 45 \text{ \AA}$ after co-assembly with **Lap**,
232 suggesting that both components co-assembled to form a higher-ordered nanostructure consisting
233 of cylindrical nanofibers and nanodisks. We also confirmed co-existence of **Lap** disks and **PAH3**
234 nanofibers by atomic force microscopy (AFM) (Fig. 2d_i-iii). The corresponding surface
235 roughness parameters Ra and Rq for the **PAH3-Lap** nanocomposites (Ra = 2.12 nm, Rq = 3.31
236 nm) are significantly higher than the values for **PAH3** nanofibers (Ra = 0.81 nm, Rq = 1.71 nm)
237 and **Lap** disks (Ra = 0.83 nm, Rq = 1.16 nm) due to the interactions between the two components
238 (Fig. 2e_i-iii). We used transmission electron microscopy (TEM) and high-resolution TEM-
239 Energy dispersive spectroscopy (HRTEM-EDS) to characterize the co-assembly. While TEM (Fig.
240 2f_i-iii) shows the diameters of **PAH3** and **PAH3-Lap** nanofibers to be $\sim 9.8 \text{ nm}$ and $\sim 12 \text{ nm}$,
241 respectively, HRTEM-EDS elemental mapping shows co-localization of the characteristic element
242 (N) on **PAH3** and the main elemental components (Si, Mg, and Na) of **Lap** (Supplementary Figure
243 S2). Such elemental co-localization is consistent with previous studies on Lap and silk co-
244 assembly.³⁷

246 **Molecular dynamic simulations of PA-Lap co-assembly**

247 *Structural optimisation of PA-nanoclay interactions*

248 In addition to the experimental evidence, we conducted molecular dynamics (MD) simulations
249 (using Material Studio 8.0 molecular modeling package by Biovia)⁵¹ to further investigate the
250 mechanism of PA-Lap co-assembly. All MD simulations were conducted using Forcite module

with COMPASS II (condensed-phase optimized molecular potentials for atomistic simulation studies) force field. The molecular structures of **PAH3** and controls **PAK3** and **PAE3** were built and optimized using the visualizer of Materials Studio 8.0. The structure of Lap is not available in the Material Studio 8.0 database, thus, we used Sepiolite ($\text{Mg}_4\text{Si}_6\text{O}_{15}(\text{OH})_{2.6}\text{H}_2\text{O}$) for this simulation due to its structural similarity with Lap. Like Lap, Sepiolite (**Sep**) is a layered hydrous magnesium silicate belonging to the 2:1 phyllosilicate family and made up of 2D tetrahedral sheet of SiO_5^{4-} . While the slight structural differences between **Sep** and **Lap** may be the limit of this simulation, we believe the simulation provides insight into the dynamic interfacial interaction between PAs and layered inorganics. To investigate the interactions between PAs and **Sep**, first we built two kind of cells; a small cell with two layers of clay (sepiolite) and one PA molecule, and a second cell (Supercell) with enlarged layers with four or ten PA molecules. In this computational elucidation, we considered both electrostatic and van der Waals terms using atom-based summation methods with a repulsive cut-off of 12.5 Å. The energy of interaction (E_{inter}) of **PAH3** with **Sep** in the cells with one, four and ten **PAH3** molecules are -736.38, -3060.72, and -5626.32 kCal/mol, respectively (Supplementary Table S2). Thus, suggesting that the total energy of the **PAH3-Sep** complex increases as further **PAH3** molecules are attracted to **Sep** to create higher-ordered nanostructures. In order to isolate the role of the imidazolium side chain of **PAH3**, we also investigated separately the interactions between a cationic **PAK3** and an anionic **PAE3** with **Sep** as controls. While interaction energy values for **PAK3-Sep** were negative, **PAE3-Sep** produces positive interaction energy. In both cases, these values increase with increasing number of molecules, suggesting that like **PAH3**, **PAK3** is attracted to the **Sep** surfaces while **PAE3** is strongly repelled.

*Force field MD simulation shows stronger interaction between **Lap** with **PAH3***

Upon insertion of the PA molecules into supercells containing **Sep** nanoclay, we further confirmed the spatio-temporal orientation of the PA molecules within the lattice (26.80 x 53.60 x 37.64 Å) of the nanoclay. With one molecule in a small cell, **PAH3** and **PAK3** molecules were attracted to the nanoclay and oriented with their positively charged head groups in close proximity to the layer while the hydrophobic tails are displayed toward the space between the layers (Fig. 3a_i-iii). As revealed in the supercells, the **PAH3** molecules accumulated on the surface of the nanoclay with the charged imidazolium side chain of the histidine residue facing the nanoclay surface (Fig.

3b_i,c_i). In contrast, the **PAK3** molecules were more evenly distributed within the lattice (Fig. 3b_ii,c_ii). The MD simulation also reveals that the negatively charged head group of **PAE3** molecules were facing towards the center of the supercells while the hydrophobic tails accumulated on the surface of the nanoclay (Fig. 3b_iii,c_iii). Taking together, there was no observable interaction between the negatively charged **PAE3** and nanoclay, whereas the cationic **PAH3** and **PAK3** preferentially interacted with the nanoclay surfaces through the charged head groups. However, **PAH3** displayed a much stronger affinity for the nanoclay to create a higher-ordered nanostructure, potentially attributable to an additional hydrogen bond contribution from the imidazolium side chain. These results demonstrate how by tuning the charged head group of PAs, it is possible to systematically optimize the supramolecular interactions between PAs and nanoclay nanomaterials, which will potentially determine gelation kinetic and mechanical properties of the resulting PA-nanoclay hydrogels on a macroscale.

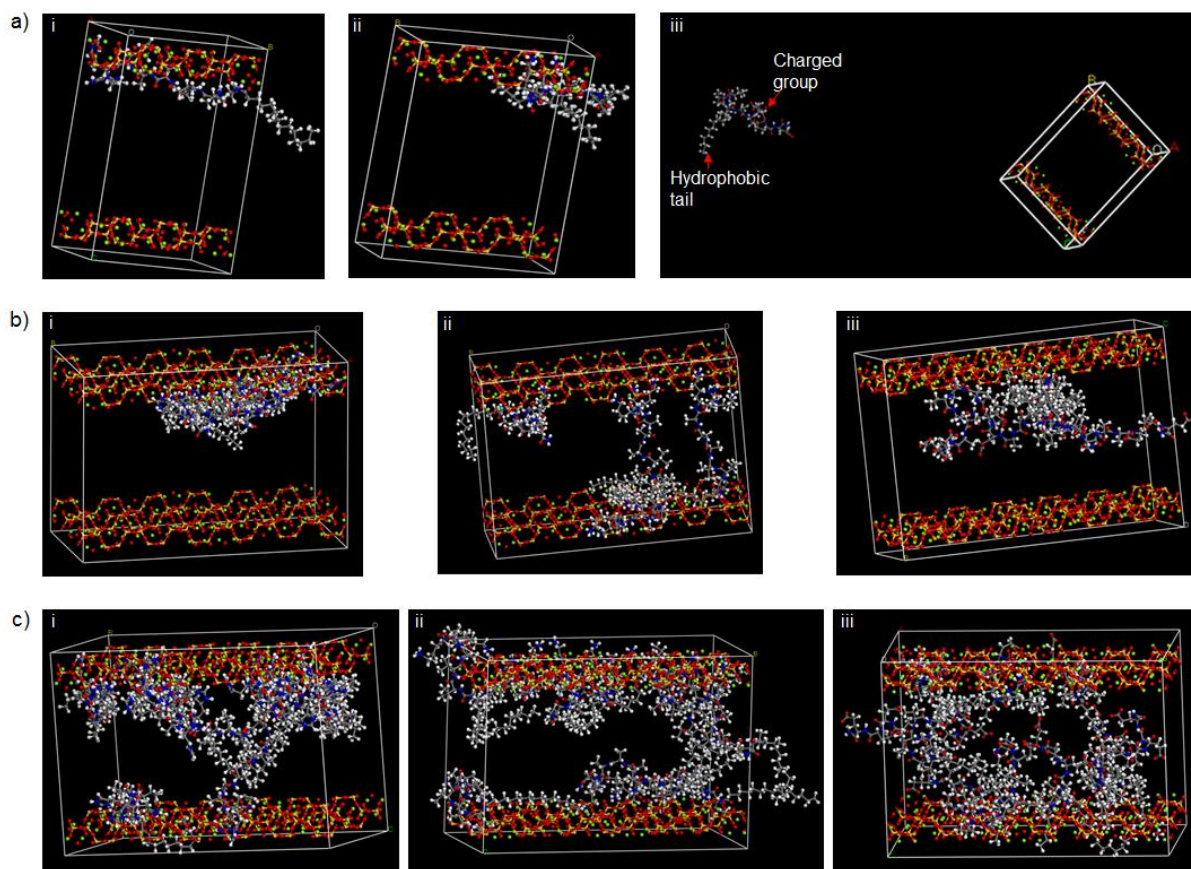


Figure 3. Molecular dynamic simulations of Laponite and PAs co-assembly. (a) Layered Sepiolite cell with - 1 molecule of (i) **PAH3**, (ii) **PAK3**, and (iii) **PAE3** after 1 ns dynamics steps. (b) Layered Sepiolite Supercell - with 4 molecules of (i) **PAH3**, (ii) **PAK3**, and (iii) **PAE3** after 1

ns dynamics steps. (c) Layered Sepiolite Supercell with - 10 molecules of (i) **PAH3**, (ii) **PAK3**, and (iii) **PAE3** after 1 ns dynamics steps.

Fabrication of PAH3-Lap nanocomposite hydrogels

Having established the underlying PA-nanoclay co-assembling mechanism, we then focused on synthesizing hydrogels using **PAH3** and taking advantage of the modular nature of our material design. Given the unique chemistry of histidine, we prepared **PAH3-Lap** hydrogels by immersing **PAH3** solution (2% w/v) into a large volume of **Lap** solution (2.5 % w/v) exfoliated with sodium salt of polyacrylic acid ($M_w = 5$ kDa, 0.06% w/v). Within 30 min of immersion, self-supported hydrogels were formed in the **Lap** solution and the hydrogel was about the size of the **PAH3** droplet (~10 mm), suggesting that the gelation was driven by a diffusion mechanism whereby **Lap** diffuses into the droplet of **PAH3** to trigger **PAH3-Lap** co-assembly, which then leads to an entangled network of **PAH3** nanofibers and **Lap** nanodisks (Fig. 4a). In contrast, immersion of **Lap** into **PAH3** did not produce stable hydrogels, which may result from a rapid diffusion of **PAH3** toward the **Lap** nanodisk suspension and inability to concentrate two components in a compartmentalized fashion. Also, when **Lap** was used without exfoliation, partial hydrogels were formed which might be attributed to electrostatic repulsion between the positive edges of **Lap** disks and the cationic imidazole side chain of **PAH3** or inhomogeneous dispersion of **Lap** in an aqueous medium. In contrast, the lysine-based analogue (**PAK3**; $\text{CH}_3-(\text{CH}_2)_{14}-\text{CONH-VVVAACKK}-\text{CONH}_2$) only formed weak hydrogels while the glutamic acid-based analogue (**PAE3**; $\text{CH}_3-(\text{CH}_2)_{14}-\text{CONH-VVVAEEEE}-\text{CONH}_2$) did not cause gelation, suggesting that the presence of histidine aromatic imidazole head groups is key to preparing stable and strong hydrogels.

Characterisation of mechanical and surface properties of PAH3-Lap hydrogels

Application of dynamic rheometry to characterise the visco-elastic properties of PA-Lap

In order to assess the impact of **Lap** on the mechanical properties of **PAH3** hydrogels, we used dynamic oscillatory rheology to measure the storage (G') and loss (G'') moduli. G' and G'' of **PAH3-Lap** hydrogels were frequency independent, with G' dominating G'' across the whole range of frequencies tested (0.1 – 50 Hz) and at constant strain γ (0.5 %) (Supplementary Figure S3). These results confirm a quasi-solid-like nature of **PAH3-Lap** hydrogels. The G' (70.89 ± 10.62 kPa) and G'' (10.54 ± 2.11 kPa) values for **PAH3-Lap** nanocomposite hydrogels were greater than

the G' (10 ± 0.51 kPa) and G'' (1 ± 0.09 kPa) values of **PAH3** hydrogels (Fig. 4b). To further confirm that supramolecular co-assembly with **Lap** can improve the stiffness of other PA hydrogels, we prepared **PAK3-Lap** hydrogels. **PAK3** is known to produce weak hydrogels ($G' \sim 1$ kPa) by charge screening. Here, we observed that **PAK3-Lap** hydrogels displayed a G' of ~ 10 kPa (Supplementary Figure S4), which is significantly lower than that of **PAH3-Lap** hydrogels (~ 70.89 kPa). This enhanced stiffness of **PAH3-Lap** over **PAK3-Lap** is expected as the aromatic imidazole side chain of the histidine residue is known to play a critical role in promoting the self-assembly of proteinaceous fibers leading to self-healable and mechanically reinforced spider fangs, sandworm jaws, or mussel byssals.⁴⁷ Therefore, we reasoned that the aromatic side chain of histidine might provide additional non-covalent interactions, making the surface free energy of adsorption (ϵ) of **PAH3** to **Lap** nanodisks greater or equal to the thermal energy ($K_B T$).⁵² This is in agreement with our initial speculation based on the molecular dynamic simulations data (Fig.3).

In addition, we carried out strain amplitude sweep measurements to determine the strain-to-break values of **PAH3-Lap** against **PAH3**. The results indicated that G' of **PAH3-Lap** decreased rapidly when subjected to a magnitude of strain beyond the critical strain value ($\gamma = 6\%$). On the other hand, G' values of **PAH3** hydrogels decreased rapidly at a much greater strain value ($\gamma = 13\%$), suggesting that **PAH3** hydrogels are more viscoelastic than **PAH3-Lap** hydrogels. Put together, the enhanced stiffness of **PAH3-Lap** over **PAH3** and **PAK3-Lap** over **PAK3** suggests that the 2D structure of **Lap** promotes a strong physical interaction between the PA nanofibers and **Lap** nanodisks (Fig. 1b). It is noteworthy that while PAs offer a powerful platform to design precise and bioactive matrixes, these materials tend to suffer from poor mechanical properties ($G' < 10$ kPa), making our organic-inorganic hybridization an attractive strategy to prepare a new class of PA-based hydrogels with dramatically improved mechanical properties ($G'_{\text{PA-Lap}} \sim 71$ kPa). This strategy has been demonstrated using **Lap** with other organic components such as silk ($G'_{\text{silk-Lap}} \sim 150$ kPa)³⁷ and dendritic molecular binders ($G'_{\text{dendron-Lap}} \sim 250$ kPa).⁴⁸

Hydrogels display thixotropic and self-recovery properties

Dynamic amplitude measurements were subsequently carried out to investigate the self-recovery or thixotropic property of **PAH3-Lap** and **PAH3** hydrogels following network rupture at high strain. We applied a high strain amplitude (100 %) to rupture the hydrogel networks followed by

1
2
3 361 a low strain amplitude (0.1 %) to investigate the rate and extent of recovery of the hydrogels.
4
5 362 Under the high strain amplitude (100 %), the hydrogels underwent internal breakage leading to a
6
7 363 significant decrease in G' and inversion of G' and G'' . The inversion signifies that the liquid-like
8
9 364 behaviour dominates the solid-like nature of the hydrogels. When the strain amplitude was reduced
10
11 365 to 0.1 %, both **PAH3** and **PAH3-Lap** hydrogels displayed fast recovery within seconds (Fig. 4c),
12
13 366 making both types of hydrogels potentially injectable. While **PAH3** hydrogels exhibited complete
14
15 367 recovery to the same initial G' , **PAH3-Lap** hydrogels exhibited enhanced recovery beyond the
16
17 368 initial G' (from 60 to 100 kPa) after the first strain cycle (Fig. 4c_green trace). Such enhanced
18
19 369 recovery has previously been reported in self-assembling hydrogels^{53, 54}, and we reasoned it is
20
21 370 suggestive of structural re-organization of the hydrogels. Macroscopically, **PAH3-Lap** hydrogels
22
23 371 were able to self-heal in air (Fig. 4d). These results suggest that **Lap** enhanced stability and
24
25 372 facilitates self-healing in **PAH3-Lap** hydrogels. The rapid self-healing process exhibited by
26
27 373 **PAH3-Lap** hydrogels may result largely from both the attachment of the imidazolium group of
28
29 374 the **PAH3** to the exfoliated **Lap** surfaces and the intrinsic propensity of **PAH3** networks to rapidly
30
31 375 recover after rupture.
32
33
34
35
36
37
38
39
40
41
42
43
44
45
46
47
48
49
50
51
52
53
54
55
56
57
58
59
60

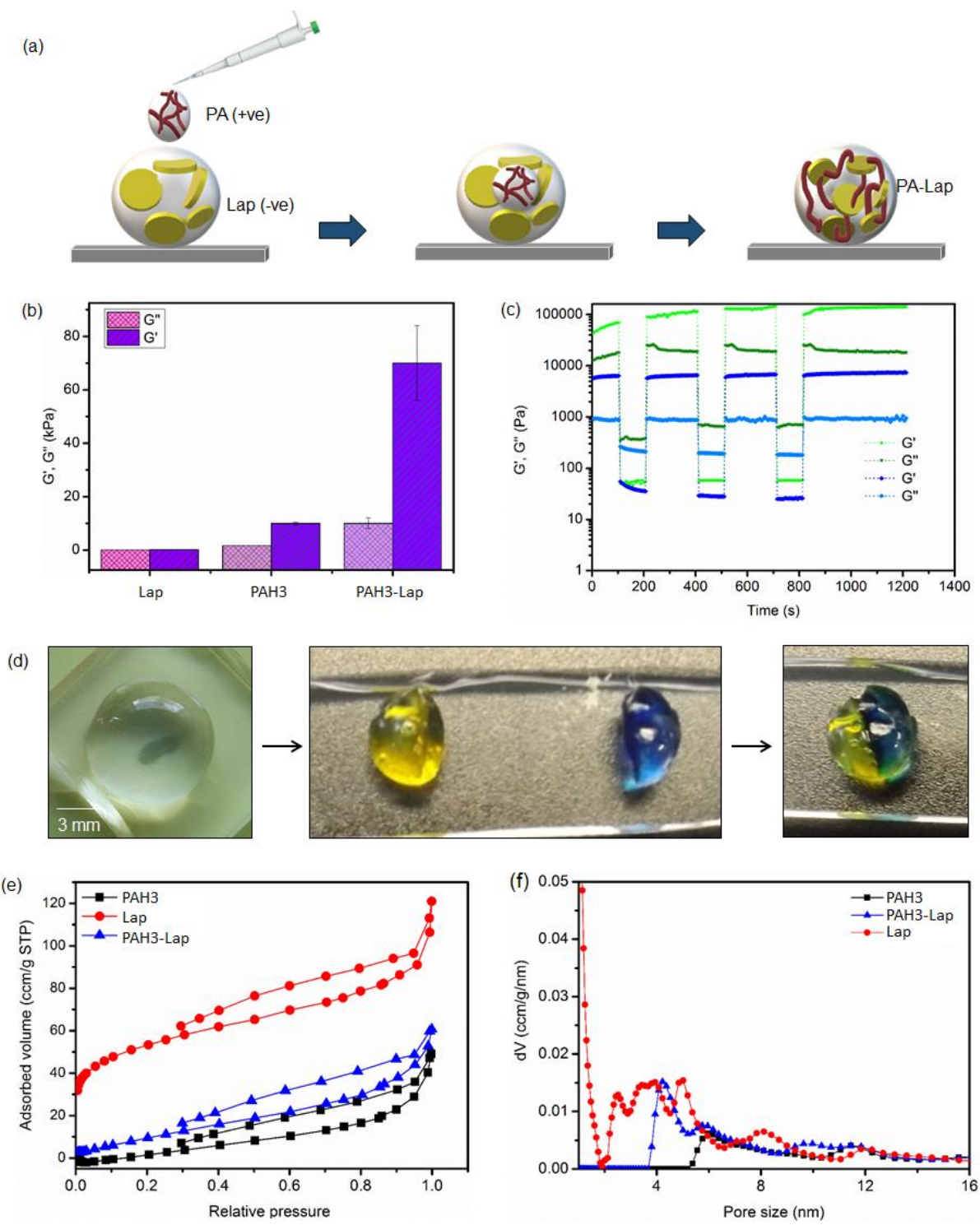


Figure 4. Surface and mechanical properties of hydrogels. (a) Schematic representation of PAH3-Lap hydrogel preparation. (b) Storage (G') and loss (G'') moduli of PAH3 and Lap compared to PAH3-Lap hydrogels. (c) Time sweep rheographs displaying thixotropic properties of PAH3 and PAH3-Lap hydrogels. (d) Optical image showing the robustness and self-healing capacity of PAH3-Lap hydrogels. (e) N₂ sorption isotherms of PAH3 (square traces), Lap

(circular traces), and **PAH3-Lap** (triangular traces) xerogels. (f) Cumulative pore volume for **PAH3**, **Lap**, and **PAH3-Lap** xerogels.

Characterisation of surface properties of **PAH3-Lap** hydrogels

Having characterized the bulk properties of **PAH3-Lap** hydrogels, we then used a nitrogen gas adsorption method based on Quenched Solid Density Functional Theory (QSDFT) to investigate the impact of PA-Lap co-assembly on surface properties including pore volumes and pore diameters. The experiments were conducted on **PAH3-Lap** dried xerogels and compared to the individual components. In all cases, the xerogels exhibited a surface profile that is consistent with type-III adsorption-desorption curves with distinct capillary condensation steps. The adsorption isotherms (volume of nitrogen per gram of materials at standard temperature and pressure (STP)) revealed that the surface areas of **Lap** and **PAH3** xerogels were 165 m²/g and 18 m²/g, respectively (Fig. 4e, Supplementary Figure S5). Upon co-assembly, the surface area (50 m²/g) of **PAH3-Lap** was higher than that of **PAH3** xerogels, implying that the surface adsorption of **PAH3** to **Lap** nanodisks considerably decreases the surface area of the **Lap** nanodisks. For **Lap**, a number of peaks which span between 0.25 – 0.78 nm (micropores), 2.00 – 6.00 nm (mesopores), and 12.00 nm (macropores) (Fig. 4f, red trace) were observed, suggesting that **Lap** displays a hierarchical polymodal pore size distributions.^{55, 56} In contrast, **PAH3** xerogel pore size distribution profiles displayed a broad peak centered at 6 nm (mesopores) and another weak peak at 12 nm, indicating that **PAH3** xerogels exhibited a uniform pore size distribution (Fig. 4f, black trace). It is important to note that the observed porosity profile for **PAH3** xerogels could be due to lyophilisation of the gels prior to analysis. The pore size distribution curves for **PAH3-Lap** showed multiple peaks centered at 4.2, 6.0, 10.0, and 12.0 nm. The peaks at 4.2 and 6.0 nm are characteristic fingerprints of **Lap** and **PAH3** xerogels, respectively (Fig. 4f, blue trace), which confirm the heterogeneity of the **PAH3-Lap** internal structure. In contrast, the peaks corresponding to the micropores of **Lap** are not apparent in **PAH3-Lap**, which suggests that surface adsorption of the **PAH3** nanofibers to the **Lap** disk removes access to the micropores by blocking them. We therefore hypothesized that the molecular diversity and heterogeneous functional groups of **PAH3-Lap** hydrogels in relation to **PAH3** hydrogels may provide an opportunity to nucleate and grow apatite crystals within the confined 3D framework of the hydrogels.

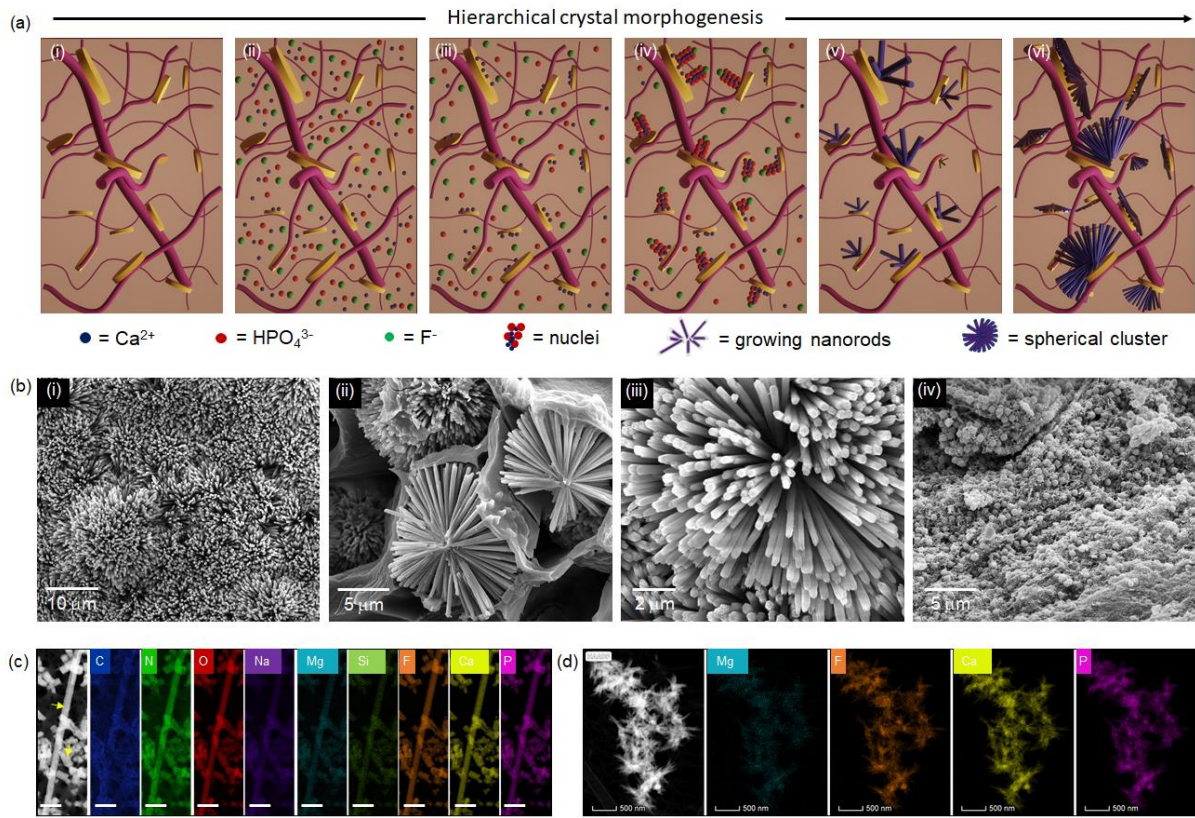


Figure 5. Biom mineralization in hydrogels. (a) Schematic representation of the biom mineralization process. **PAH3-Lap** hydrogel was immersed in a mineralizing bath followed by a gradual diffusion of the ionic precursors into the hydrogel cavity (i), which resulted in an initial electrostatic binding of calcium (Ca^{2+}) ions to the **Lap** surface (ii). Further association of phosphate (HPO_4^{3-}) and fluoride (F^-) ions with the Lap- Ca^{2+} complex produces nuclei (iii) that developed into oriented nanorods in a time-dependent manner (v), which organize hierarchically into spherical clusters (vi). (b) Scanning electron micrographs showing (i) dense crystal formation on the surface of a **PAH3-Lap** hydrogel, which are (ii, iii) organized into spherical clusters of nanorods within the cavity of the hydrogels after 8 days in mineralizing solution. In contrast, **PAH3** hydrogels mineralized but spherical and amorphous crystals were formed (iv). (c) HRTEM-EDX elemental mapping of nanorods formed in **PAH3-Lap** hydrogels after 8 days. Yellow arrows indicate fluoridated hydroxyapatite nanorods. Elemental mapping of the nanorods shows carbon C (blue), nitrogen N (green), oxygen O (red), sodium Na (purple), magnesium Mg (cyan), silicon Si (green), fluorine F (orange), calcium Ca (yellow), and phosphorus P (pink). Scale bar: 100 nm. This was contrasted with the morphology of the (d) needle-like crystals that formed in **PAH3-Lap** hydrogels within 2 h of incubation in mineralizing solutions.

PAH3-Lap hydrogels to guide *in situ* mineralization

Features that make organic-inorganic hydrogels an ideal model for biom mineralization

Hydrogels have been harnessed as structural frameworks to elucidate the origins of biological control over crystal morphology, orientation, and matrix incorporation.³ These materials display

(i) volumetric confinement to control crystal growth, (ii) nanoporosity to control diffusion rates, capacity to tune concentrations and supersaturation of solutes, and (iii) internal nanostructures with high surface area to template crystal growth.^{3, 57} Unlike the classical mechanism of atom or molecule mediated growth of single crystals, the particle mediated growth and assembly mechanisms leading to the formation of single crystals have been recognized as emerging non-classical biomineralization processes.⁵⁸ This phenomenon is believed to result from both the free-energy landscapes and reaction dynamics that govern particle-particle interactions.⁵⁹⁻⁶¹ Such reaction dynamics might account for the impressive mineral deposition recently observed by Paul and co-workers using DNA-Laponite hybrid hydrogel coatings on bone allografts.³⁶ Therefore, we hypothesized that the surface area, functional groups, and structural anisotropy of **Lap** nanodisks can be harnessed in **PAH3-Lap** hydrogels to control the energy landscape at the substrate-nuclei interface during biomineralization in a time-dependent manner, leading to the formation of multi-inorganic-organic nano-objects.

To test this hypothesis, we used a known mineralizing solution to nucleate and trigger the growth of fluoridated hydroxyapatite nanocrystals.¹⁰ The **PAH3-Lap** hydrogels were submerged in the mineralizing solution (20 mL) and kept at 37 °C (Fig. 5a). We observed that the transparent **PAH3-Lap** hydrogels became cloudy within 8 days of incubation (Supplementary Figure S6), suggesting its high mineralization capacity. In contrast, **PAH3** hydrogels remained less opaque, indicating less mineralization than **PAH3-Lap** hydrogels. In order to confirm that this enhanced mineralization was due to the presence of **Lap**, we added **Lap** solution alone to the mineralizing solution and investigated crystal formation. Interestingly, **Lap** suspension exhibited white precipitates after 8 days of incubation, suggesting that **Lap** is able to drive nucleation and growth of apatite crystals. These results are potentially consistent with the ability of **Lap** nanodisks to act as catalysts for the formation of mineralized matrixes both in *in vitro* and *in vivo*.³²⁻³⁴ Similarly, silica hydrogels have previously been used to drive the formation of hematite ($\alpha\text{Fe}_2\text{O}_3$) into hierarchical mosaic crystals displaying hierarchical structures inaccessible in solution-grown controls, indicating that silicate materials display functionalities that promote heterogeneous nucleation and growth of crystals.⁶²

Lap nanodisks are essential for nanorod formation

Scanning electron microscopy (SEM) was used to examine the mineralization within the hydrogels. SEM micrographs of **PAH3-Lap** xerogels revealed the presence of high-aspect ratio apatite nanorod crystals (~ 50 nm in cross-sectional diameter) on the surface of the mineralized hydrogels after 8 days in the mineralizing solution (Fig. 5b_i). These apatite nanorods were organized hierarchically into well-defined microscopic clusters, which resemble mesocrystals.⁶³ The clusters grew symmetrically and to similar sizes up to microns in diameter in “confined pockets” within the hydrogels (Fig. 5b_ii-iii). We hypothesize that these cluster structures are formed by the diffusion of ionic mineralization precursors through the **PAH3-Lap** hydrogel, random nucleation across the internal walls of the hydrogel, and subsequent symmetric growth of apatite nanorods along the precursor-crystal interface (Fig. 5c). This process of crystal growth and entrapment within integrated hybrid materials has been regarded as nanoscale incarceration by Mann.¹⁷ In contrast to this nanorod and microcluster organization within **PAH3-Lap** hydrogels, we observed spherical nanocrystals (diameter ~50 nm) in **PAH3** hydrogels, which are reminiscent of previous studies by Stupp and colleagues.⁶⁴ Based on these results, we propose that the integrated nanofibers and nanodisks within **PAH3-Lap** hydrogels provide a 3D organic-inorganic framework of heterogeneous nucleation sites for hierarchical mineralization. To explore the possibility that **Lap** is acting as a catalyst for mineralization in the **PAH3-Lap** hydrogels, we hybridized **Lap** with **PAK3** knowing that **PAK3** does not induce mineralization of apatite in its own right. In this case, we again observed formation of the both nanorods and nanospheres within the hydrogels after 8 days of incubation (Supplementary Figure S7). Thus, suggesting that the presence of **Lap** nanodisks in PA-based hydrogels played a key role in the nucleation and growth of crystals within the hydrogels.

Elemental mapping to elucidate co-localisation of Lap and hydroxyapatite

Given the hierarchical nanorod-cluster mineralization within **PAH3-Lap**, we then investigated nanorod crystal formation in further detail. First, to verify interactions between **Lap** nanodisks and the mineralization ionic precursors, we used HRTEM-EDS to map the elemental composition of the mineralized **PAH3-Lap** hydrogels. HRTEM images confirmed the formation of the ~50 nm diameter hexagonal nanorod crystals in the **PAH3-Lap** hydrogels after 8 days of incubation (Fig 5c). Also, the HRTEM-EDS mapping revealed co-localization of carbon (C), nitrogen (N), oxygen (O), sodium (Na), magnesium (Mg), silicon (Si), fluoride (F), calcium (Ca), and phosphorous (P)

along the nanorods, which suggests the incorporation of dissolved **PAH3** and **Lap** into the nanocrystals during growth. To gain insight into the early stage of this mineralization phenomenon, we examined the morphology and elemental composition of the crystals obtained after 2 h incubation period in the mineralizing solution. HRTEM-EDS micrographs of **PAH3-Lap** hydrogels following a 2 h incubation period revealed an outward growth of the spherical clusters comprising the nanorods with co-localized elemental components of **PAH3-Lap** hydrogels (Fig. 5d). Moreover, the nanorods appeared to be growing in the direction of the **PAH3-Lap** hydrogel nanofibers (Supplementary Figure S8a), which suggests that the orientation of the nanofiber-nanodisk hybrid might be playing a key role in directing the hierarchical nanorod growth. Also, the white particles that sediment in the **Lap** solution were analyzed using HRTEM-EDS, which revealed the formation of agglomerated nanorods with elemental mapping showing both **Lap** characteristic elements and ionic precursors for mineralization (Supplementary Figure S9). These results indicate that **Lap** might be serving as an essential template for nanorod growth within the organic-inorganic hydrogels due to its 2D ultrathin structure and surface chemistry.

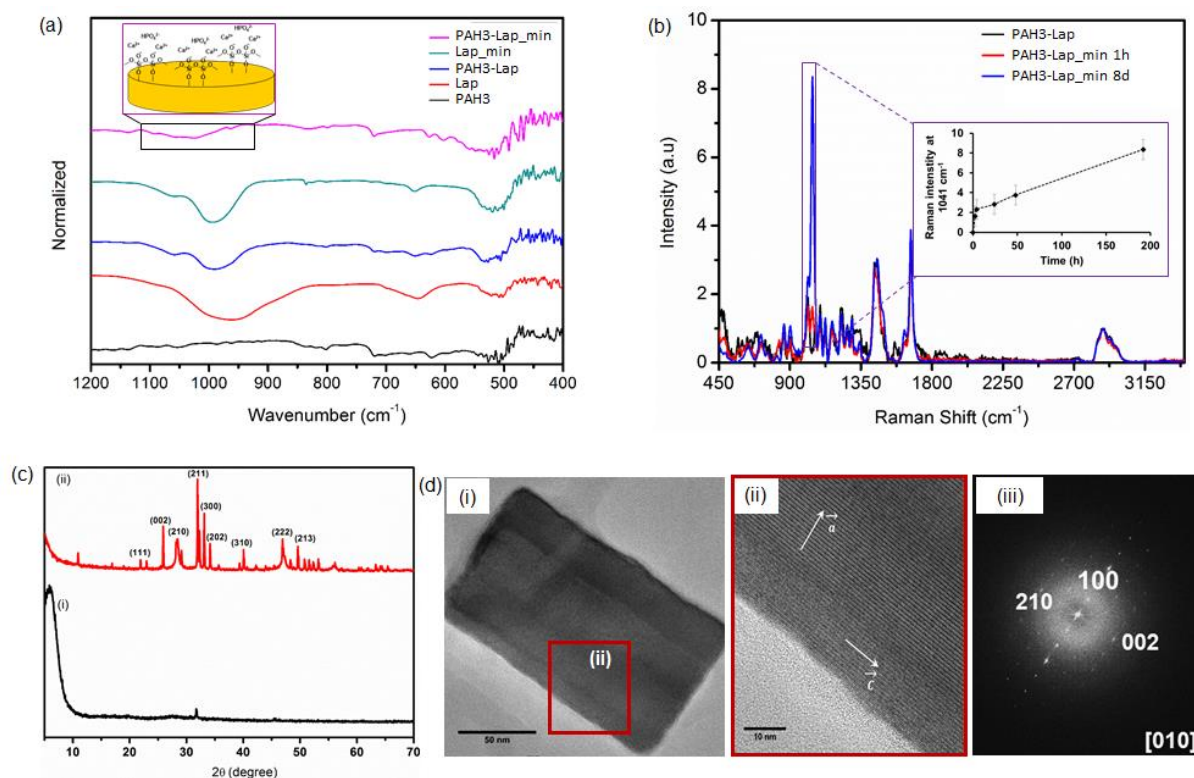


Figure 6. Characterisation of biomineralization. Raman spectroscopy was used to monitor extent of mineralization at various time intervals. (a) FTIR spectra indicating **Lap** silica oxide layer participation in biomineralization. (b) Normalized Raman spectra of unmineralised **PAH3-Lap** hydrogels and **PAH3-Lap** mineralized for 1 and 8 days. The inset is a plot of 1047 cm^{-1} signal

intensity versus mineralization time. (c) X-ray powder diffraction (XRD) crystallographic profiles of mineralized (red trace) and unmineralized (black trace) **PAH3-Lap** hydrogels after 8 days of incubation in mineralizing solution. (d) (i) HRTEM image of hydroxyapatite nanorods formed in **PAH3-Lap** hydrogels, (ii) Enlarged selected area (red square) of HRTEM image of nanorods and (iii) FFT patterns of crystals viewed from the [010] crystallographic direction.

*FTIR confirms hydrogen bond-driven interactions between **Lap** and biominerals*

Using Fourier transform infrared (FTIR) spectroscopy, we then investigated the mechanism of interaction between **Lap** and the ionic precursors present in the mineralizing solution. With the technique we also attempted to verify the identity of the apatite nanorods. According to the FTIR spectra (Fig. 6a), the band at 970 cm^{-1} corresponds to Si-O-Si of **Lap**. This band shifts from 970 cm^{-1} to 985 cm^{-1} in **PAH3-Lap** hydrogels, which suggests hydrogen-bonding interactions between **PAH3** and **Lap**. Such red-shift in the Si-O-Si band of **Lap** has previously been observed in polymer-Lap composite hydrogels.⁶⁵ After incubating **PAH3-Lap** in the mineralizing media for 8 days, the band became broader and was further shifted to a higher frequency (*ca* 1022 cm^{-1}). Thus, we hypothesized that the mineralized **PAH3-Lap** hydrogels interacted non-covalently with the Si-OH layer of **Lap**. To verify this, we incubated a **Lap** suspension in the mineralizing media under the same conditions for 8 days. The band of Si-OH shifted from 970 to 995 cm^{-1} , confirming **Lap** as an active catalyst for mineralization in **PAH3-Lap** hydrogels.

Time-resolved evolution of nanocrystals and associated fingerprints to understand mechanisms of biomineralization

Given the distinctive functional groups of **Lap**, **PAH3**, and the mineralized nanorods, Raman spectroscopy was used to elucidate their molecular composition within mineralized **PAH3-Lap** hydrogels. Furthermore, by taking advantage of the fingerprints of phosphate functional groups on the nanorods, we monitored the kinetics of crystal growth in **PAH3-Lap** hydrogels. The Raman spectra of the **PAH3-Lap** hydrogels mineralized for 8 days revealed vibrational frequencies corresponding to the internal PO_4^{3-} mode. The vibrational frequencies of the PO_4^{3-} were found to be $\nu_1 = 960\text{ cm}^{-1}$ and $\nu_3 = 1047\text{ cm}^{-1}$ (Fig. 6b). These frequencies correspond to the characteristic symmetric P-O stretching modes and the triply degenerate asymmetric P-O stretching modes, respectively.⁶⁶ Peaks at 1450 cm^{-1} (C=C stretch of imidazole side chain) and 1675 cm^{-1} (C=O stretch, amide band I) correspond to peptide vibrations from **PAH3** while the peak at 1010 cm^{-1} corresponds to Si-O vibrational stretch from **Lap** present in the **PAH3-Lap** hydrogels. The amide

band I at 1675 cm^{-1} further confirms the intrinsic β -sheet conformation of **PAH3** nanofibers in the co-assembled **PAH3-Lap**.⁶⁷ By comparing this amide band I before and after mineralization, we observed no significant changes in the conformation of **PAH3** nanofibers. Thus, suggesting that the **PAH3** nanofibers maintained their spatial organization under the mineralization event.

We monitored the kinetics of crystal growth in the **PAH3-Lap** hydrogels by observing the regions of the Raman spectra corresponding to the triply degenerate asymmetric P-O stretching modes ($\nu_3 = 1047\text{ cm}^{-1}$). At time $t = 0$ (before mineralization), no Raman peak was apparent in this region. After mineralization for 1 h, there was an emergence of the P-O stretching mode that featured two sharp peaks at 1005 and 1047 cm^{-1} (Fig. 6b, Supplementary Figure S10). The relative intensity of the 1047 cm^{-1} peak signal (all spectra were first normalized with respect to the C-H signal intensity at $2800\text{--}3000\text{ cm}^{-1}$) increased rapidly within 4 h of mineralization and steadily afterward until the 8-day time-point (Fig. 6b_inset, Supplementary Figure S10), indicating a two-phase crystal growth. Elemental analysis of the two stages of crystal growth revealed a Ca/P ratio of 1.45 and 1.65 for the nanorods obtained at 4 h and 8-day time-points, respectively (Supplementary Figure S8d). The former Ca/P ratio is indicative of an amorphous calcium phosphate while the latter is characteristic of a hydroxyapatite crystal. Thus, the two-stage crystallization events exhibited an initial amorphous precursor phase, which steadily underwent a slow interaction with the mineralization ionic species diffused into the **PAH3-Lap** hydrogels, leading to a linear rate of growth to attain the hydroxyapatite composition with Ca/P ratio 1.65. Similarly, Raman spectra for **PAH3** hydrogels mineralized for 8 days also displayed the key PO_4^{3-} fingerprints ($\nu_1 = 960\text{ cm}^{-1}$, $\nu_3 = 1047\text{ cm}^{-1}$) of hydroxyapatite formed in **PAH3-Lap** hydrogels as well as a Raman peaks at 564 cm^{-1} (Fig. 6b), which corresponds to ν_4 bending mode characteristic of PO_4^{3-} in amorphous calcium phosphate.⁶⁷ We also used elemental analysis to show that the Ca/P ratio is 1.1 for the amorphous calcium phosphate formed in the **PAH3** hydrogels (Supplementary Figure S12).

*XRD and other physical analysis techniques confirm crystallographic direction of crystal growth in the **PA-H3-Lap** hydrogels*

The X-ray diffraction pattern of the mineralized **PAH3-Lap** hydrogels compared to the unmineralized **PAH3-Lap** hydrogels indicated that the nanocrystals formed after 8 days were crystalline (Fig. 6c). More so, the diffraction peaks (002) at $2\theta = 25.8^\circ$, (211) at $2\theta = 31.8^\circ$, (300)

at $2\theta = 32.8^\circ$, (202) at $2\theta = 34.2^\circ$, and (222) at $2\theta = 46.9^\circ$ (Fig. 6c_ii) are consistent with the peaks for fluoridate hydroxyapatite.⁵⁷ Furthermore, the sharp 002 peak indicated that the nanorods were oriented along the c axes, which is reminiscent of nanocrystal growth in both dental enamel and bone.⁶⁸ A closer look at the HRTEM images of the mineralized **PAH3-Lap** hydrogels confirmed that the nanorods assumed a preferred orientation along the c axes of the fluoridated hydroxyapatite (Fig. 6d_i-ii). Also, the fast Fourier transform (FFT) patterns viewed from the [010] crystallographic direction are consistent with the XRD data and HRTEM images, indicating that the crystal lattices were only observed in the nanorods with long axes along the direction corresponding to the reflection area (Fig. 6d_iii). These results further confirm that the c axes of the crystal lattices were mainly aligned along the long axes of the nanorods. Although, the potential of **Lap** to trigger cascades of cell signaling that mediate bone formation *in vivo* is well-known,²⁸ these results showcase the potential of **Lap** nanodisks as efficient templates to guide nanocrystal growth via a non-classical particle attachment mechanism and in a hierarchical manner.

Evaluation of biocompatibility of mineralised PAH3-Lap hydrogels

The biological relevance of **PAH3** as well as mineralized and unmineralized **PAH3-Lap** hydrogels as functional biomaterials was assessed *in vitro* by seeding human bone marrow stromal cells (hBMSCs) on the hydrogels. As shown in Fig. 7a, live skeletal cells stained with calcein AM were predominantly visible on the hydrogels after 7 days in culture, indicating excellent cytocompatibility across the hydrogels. However, hBMSCs proliferated significantly more on the mineralized **PAH3-Lap** hydrogels compared to the **PAH3** and unmineralized **PAH3-Lap** hydrogels, as well as on tissue culture plastic (TCP) (Supplementary Figure S13). To further assess the biological functionality of the hydrogels *ex vivo*, we used the chorioallantoic membrane (CAM) assay of the chick embryo, to examine tissue integration and blood vessel and extracellular matrix formation as previously published.⁶⁹ Histological analysis of the implanted **PAH3**, unmineralised, and mineralised **PAH3-Lap** hydrogels after 7 days demonstrated that the hydrogels fully integrated within the CAM (Fig. 7b-i). However, while blood vessels were only visible on the surface of the **PAH3** hydrogels (Fig. 7b_i), both unmineralised and mineralised **PAH3-Lap** hydrogels exhibited blood vessels growing within (Fig. 7b_ii-iii), indicating a higher capacity of neovascularization. Using Goldner's and von Kossa staining, we confirmed extensive mineral deposition in the mineralized **PAH3-Lap** (**PAH3-Lap-min**) hydrogels (Fig. 7c_iii) in comparison

to unmineralised hydrogels (Fig. 7c_ii). No mineral deposition was apparent in the blank eggs (Fig. 7c_iv). These results suggest that the **PAH3-Lap** hydrogels can serve as robust multifunctional matrices with the capacity to promote cell growth, trigger hierarchical mineralization and bone tissue formation, and promote vascularisation.

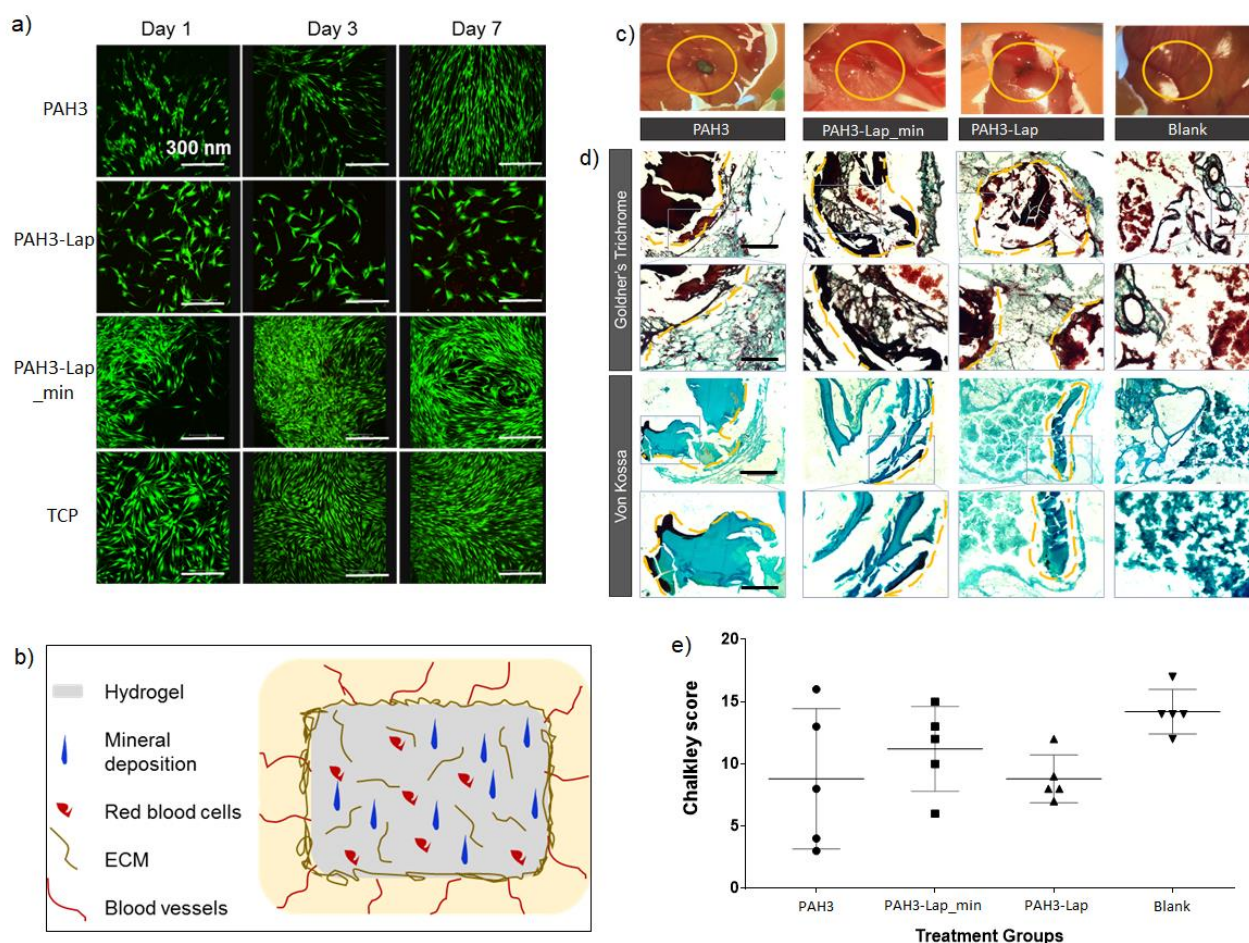


Figure 7. Biological applicability of PAH3-Lap hydrogels. (a) The in vitro applicability of the hydrogels was assessed by a LIVE/DEAD assay to test cell viability and proliferation of hBMSC on the hydrogels. The results revealed that cell viability and proliferation on mineralized **PAH3-Lap** hydrogels are more than those of cells growing on tissue culture plastic (TCP) for 7 days. (b) Schematics of CAM implantation of hydrogels. Hydrogels promote mineral deposition, red blood cell infiltration, and ECM and blood vessels formation. (c) Optical image of CAM implanted hydrogels. **PAH3** hydrogels implanted in CAM were surrounded by blood vessels in close proximity of the chorioallantoic membrane. Both **PAH3-Lap** and **PAH3-Lap.min** hydrogels were highly integrated with the chorioallantoic membrane with blood vessels penetrating the implanted hydrogels. (d) Histological analysis of CAM implanted hydrogels. Mineral deposition was found limited to the outer region of the implanted **PAH3** hydrogels. Limited mineral deposition was observed in proximity of **PAH3-Lap** hydrogel-membrane interface. Mineral deposition was found extensively within the **PAH3-Lap.min** hydrogels. Both **PAH3-Lap** and **PAH3-Lap.min**

hydrogels were extensively invaded by red blood cells. Blank samples were extensively penetrated by blood vessels but no mineral deposition. (e) Chalkley score of **PAH3**, **PAH3-Lap**, **PAH3-Lap_min**, and blank controls samples. Statistical significances were assessed by one-way ANOVA. Mean \pm S.D. n=5. Scale bar = 100 μ m.

3. Conclusion

We have developed a new co-assembling organic-inorganic hydrogel platform for *in vitro* crystal growth mediated by a particle attachment mechanism within a 3D supramolecular confined framework. The design strategy hinges on electrostatic interactions between **Lap** nanodisks and cationic **PAH3** molecules to integrate the intrinsic properties of the organic and inorganic components into distinctive organic-inorganic hydrogel structures. The resulting materials displayed high surface area, high mechanical properties, and self-healing properties. Furthermore, the co-assembling PA-Lap hydrogel displayed a nanoscale architecture that served as confined spaces for the hierarchical growth of hydroxyapatite from ordered nanorods into well-defined spherical clusters. The study explores this mineralization mechanism as a biomimetic 3D model to modulate nucleation and spatio-temporal organisation of fluoridated hydroxyapatite. This model was used to understand the role of both **Lap** nanodisks and **PAH3** nanofibers within **PAH3-Lap** hydrogels in guiding the growth of the hydroxyapatite nanorods across multiple length scales. At the atomic level, the mineralization of **PAH3-Lap** depended on a diffusion-driven process where local ionic concentration and supersaturation are mediated by supramolecular interactions with **Lap**. Furthermore, the nanoscale architecture of the **PAH3-Lap** hydrogels facilitated incarceration of the newly formed nanorod crystals and subsequent growth into the distinctive spherical clusters at the microscale. Remarkably, these mineralized **PAH3-Lap** nanocomposite hydrogels outperformed all control groups in supporting cell growth, and stimulation of cell ingress, blood vessel infiltration, ECM production, and mineral deposition in a CAM model. In addition to these advantages, the shear-thinning property of the system makes it a suitable material to serve as a bioink for 3D printing applications. Overall, this study presents a new nanotechnology approach to the design of integrated and higher-ordered self-assembling nanomaterials with potential widespread applications in regenerative medicine.

Experimental methods

Zeta potential (ζ)

All ζ -potential measurements were performed after resuspension of the PAs at a concentration of 0.1% w/v in ultrapure water. After loading the samples in folded capillary cells, measurements were performed at 25°C using a ζ -sizer instrument (Nano-ZS Zen 3600, Malvern Instruments, UK). For each PA, three separate samples were measured with at least five runs per sample.

Circular dichroism spectroscopy

Circular dichroism (CD) was measured with Chirascan™ circular dichroism spectrometer (Applied Photophysics Limited, UK) using quartz cell with 1 mm path length and the following parameters: data pitch – 0.5 nm, scanning mode – continuous, scanning speed – 100 nm/min, bandwidth – 2 nm and accumulation – 5. All CD data are presented as ellipticity and recorded in millidegree (mdeg). CD measurements were performed on aqueous solutions of **PAH3** (0.1% w/v), Lap (0.25%) and their mixtures. CD spectra were obtained by signal integrating 3 scans, from 190 to 260 nm at speed of 50 nm/min. Data were processed by a simple moving average and smoothing method.

Small-Angle Neutron Scattering (SANS) analysis of hydrogel nanostructures

Synchrotron small-angle neutron scattering (SANS) measurements were performed on the fixed-geometry, time-of-flight LOQ diffractometer (ISIS Neutron and Muon Source, Oxfordshire, UK). A white beam of radiation with neutron wavelengths spanning 2.2 to 10 Å was enabled access to Q [$Q = 4\pi\sin(\theta/2)/\lambda$] range of 0.004 to 0.4 Å⁻¹ with a fixed-sample detector distance of 4.1 m. The cuvettes were mounted in aluminium holders. Time taken for each measurement was approximately 30 minutes. All scattering data were normalized for the sample transmission, the backgrounds were corrected using a quartz cell filled with D₂O and the linearity and efficiency of the detector response was corrected using the instrument-specific software.

Atomic Force Microscopy (AFM)

AFM was performed on the Bruker Multimode 8 AFM with a Nanoscope V controller using PeakForce Tapping mode with a ScanAsyst Air cantilever (spring constant 0.4N/m). The cantilever was calibrated using the automated ‘no touch’ calibration routine built into the software.

Solutions of **PAH3** (0.01% w/v, 40 μ L), **Lap** (0.025% w/v, 40 μ L), and **PAH3/Lap** mixtures were dropped onto freshly cleaved mica surfaces. The samples were air dried at room temperature for 24 h and imaged with a PeakForce setpoint of 500 pN with a PeakForce amplitude of 30 nm and frequency of 4 kHz. Images were acquired at 512x512 pixels at a line rate of 2.8Hz. The height images were processed in the Nanoscope Analysis software after using 1st order flattening to remove tilt. Images were processed in Nanoscope 1.7.

Transmission Electron Microscopy (TEM) and High Resolution TEM (HRTEM)

Aqueous solutions of **PAH3** (0.01% w/v) and **Lap** (0.025% w/v, exfoliated with 0.0068% w/v ASAP) were dissolved ultrapure water. Similarly, mixtures of **PAH3** (0.02% w/v) and **Lap** (0.5% wt/v) were also prepared. Samples were mounted on copper TEM plasma etched holey carbon-coated copper grid (Agar Scientific, Stansted, UK). The grids were immersed in the sample solutions for five minutes. Excess was removed on filter paper before incubation with 2% uranylacetate solution for 30 seconds. Grids were then washed with ultrapure water for 30s and air dried for 24h at room temperature. Bright-field TEM imaging was performed on a JEOL 1230 Transmission Electron Microscope operated at an acceleration voltage of 80 kV. All the images were recorded by a Morada CCD camera (Image Systems). At least three images were taken per samples for further analysis. High resolution transmission electron microscope (HRTEM) images, selected area electron diffraction (SAED) patterns, scanning transmission electron microscope (STEM) images and energy dispersive X-ray spectroscopy (EDS) spectrum images were obtained with a FEI Talos F200X microscope equipped with an X-FEG electron source and Super-X SDD EDS detectors. The experiment was performed using an acceleration voltage of 200kV and a beam current of approximately 1 nA. TEM Images were recorded with a FEI CETA 4k x 4k CMOS camera. STEM images were acquired with HAADF and BF detectors.

Preparation of hydrogels

Aqueous solution of **Lap** (2.5% w/v) was prepared by adding the requisite amount of Laponite powder to a stirred suspension of ASAP (0.06% w/v) in ultrapure water. The **Lap** suspension was sonicated for 30 min until clear transparent sample was obtained. Aqueous solutions of **PA** (2% w/v) were prepared in HEPES buffer. **PA-Lap** hydrogels were prepared by injecting solution of **PA** (20 μ L) into a larger volume of **Lap** (100 μ L). Gelation was allowed to proceed overnight at

room temperature. Hydrogels of **PAH3** (2% w/v) were prepared by basifying aqueous solution of **PAH3** with NaOH (1M).

Dynamic rheological measurements

Rheological measurements were performed using a Discovery Hybrid Rheometer, Rheo-DHR3 (TA Instruments). All data were collected at 25 °C. The preformed hydrogels were added to the center of the bottom plate and the top parallel plate (with 8 mm diameter) was lowered to a gap of 100 μm . The amplitude sweep measurements were performed between 0.1 and 50 % strain at constant frequency (1 Hz). Similarly, frequency sweep rheographs were obtained between 0.1 and 20 Hz at constant strain (0.5%). Self-healing was assessed initially at 0.1% strain for 100 s, then at 100% strain for 200 s, 0.1% strain for 200 s, 100% strain for 200 s and 0.1% strain for 400 s.

Characterization of surface properties of xerogels

Nitrogen sorption isotherms of the lyophilized xerogels were measured at 77 K using an Autosorb-IQ system (Quantachrome Instrument, USA). Before measurements, the samples were degassed in a vacuum at 120 °C overnight. The specific surface areas (S_{BET}) were calculated by the multipoint Brunauer-Emmet-Teller method using adsorption data in a relative pressure range from 0.04 to 0.2, and the pore-size distribution was calculated based based on quenched solid density function theory (QSDFT) using the adsorption branches of isotherms assuming slit and cylindrical pores geometries. By using the Barrett-Joyner-Halenda (BJH) model, the mesoporous surface areas (S_{BJH}) were calculated from the adsorption line. The microporous surface areas (S_{DR}) were calculated from the adsorption line by the Dubinin–Radushkevich (DR) model.

Biom mineralization of hydrogels

The mineralizing solutions were prepared as previously reported by Elsharkawy et al.² Briefly, an aqueous suspension of hydroxyapatite powder (2 mM) and sodium fluoride (2 mM) was prepared in deionized water with continuous stirring. Then, 69% nitric acid was added dropwise to the suspension to aid a complete dissolution of the hydroxyapatite precipitates at pH 2.4. Thereafter, an aqueous solution of ammonium hydroxide (30%) was added dropwise to the hydroxyapatite solution until it reaches pH 6. Various hydrogels were then immersed in the hydroxyapatite solutions and incubated for eight days at 37 °C using a temperature-controlled incubator (LTE

Scientific, Oldham, UK).

754

755 **Monitoring of biomineralization process via Raman Spectroscopy**

756 All Raman analysis was carried out on a confocal WITEC Alpha300 system utilising a 785 nm
757 laser and a 20× (S Plan Fluor, NA 0.45, ELWD) objective lens. Raman scatter was collected in a
758 backscattering geometry. A small amount of each sample was placed on a microscope glass slide
759 which had been previously cleaned with a methanol-soaked tissue, with a new slide used for each
760 sample. The incident laser power was constant for all samples at 63 mW. No signal loss was
761 observed, for example due to photobleaching or carbonisation, when samples were irradiated on
762 the same spot in triplicate with integration times ranging from 10 s to 60 s. All spectra processing
763 was performed using SpectraGryph 1.2 involving: 1) cosmic ray removal, 2) background
764 correction and then 3) subsequent normalization. An advanced baseline correction protocol
765 available in the SpectroGryph software was applied which fits a polynomial curve to the spectral
766 regions where there is no Raman peak and enables subtraction of the variable y-offset associated
767 with the luminescence background. To enable comparison of the relative changes in the Raman
768 intensity of the 1047 cm^{-1} peak in Figures 6 and S10, all spectra were normalized with respect to
769 the peak intensity in the 2800-3000 cm^{-1} region. This approach was adopted as the integration time
770 was varied between samples to optimize the signal to noise ratio alongside variation in background
771 luminescence with mineralization times. However, the C-H vibrational spectral shape across 2800-
772 3000 cm^{-1} remained relatively unchanged for each sample and the Raman peak intensity was also
773 observed to change proportionally with integration time in this region. For each measurement,
774 multiple spectra were acquired across the sample with the focus depth also optimized, which
775 revealed good uniformity and ensured that the spectra presented are representative of the sample.

776

777 **Synthesis and purification of peptide amphiphiles**

778 The peptide amphiphiles (PAs) were synthesized using solid phase peptide synthesis (SPPS) on
779 Liberty Blue automated microwave peptide synthesizer (CEM, UK). The standard 9-
780 fluorenylmethoxycarbonyl (Fmoc) protection chemistry on a 4-methylbenzhydrylamine (MBHA).
781 Rink Amide resin (Novabiochem Corporation, UK) was employed. PAs were purified using a
782 preparative High-Performance Liquid Chromatography (Waters, USA) with reverse-phase
783 Xbridge C18 column (Waters, USA) and water/acetonitrile (0.1% NH_4OH or TFA) binary mobile

phase.

785

786 **Chick chorioallantoic membrane (CAM) assay**

787 *Implantation, extraction and Chalkley score*

788 Animal studies were performed in accordance with the guidelines and regulations laid down in the
789 Animals (Scientific Procedures) Act 1986. CAM model was carried out in accordance with Home
790 Office Approval, UK (Project license – PPL P3E01C456). Chicken eggs were acquired from
791 Medeggs (Norfolk, UK). Eggs were stored in Hatchmaster incubator (Brinsea, UK) at 37 °C in a
792 60 % humidified atmosphere and 1 h rotation. To ensure the maintenance of a humidified
793 environment in the egg incubator deionised water (DW) was supplemented every two days.
794 Implantation was carried out after 7 days of incubation. To assess embryo viability and
795 development eggs were candled. A window of 1cm² was created with a scalpel onto the egg shell
796 exposing the chorioallantoic membrane. Hydrogels were implanted and the window sealed with a
797 sterile Parafilm strip (Bemis™, Parafilm M™, Laboratory Wrapping Film, Fisher Scientific, UK).
798 Eggs were return to the Hatchmaster incubator for 7 days (37 °C in a 60 % humidified atmosphere)
799 without rotation. Chalkley scoring was used as previously described³ to quantify infiltration of
800 blood vessels through the implanted scaffolds. Implants and blank controls were observed *in situ*
801 under a stereo light microscope. A total of five independent counts obtained from the number of
802 vessels fitting with the Chalkley graticule projected onto the samples were registered.

803

804 *Histological analysis*

805 Integrated hydrogel samples were extracted and fixed in 4 % paraformaldehyde (PFA) overnight.
806 Samples were further embedded in optimum cutting temperature (OCT embedding matrix,
807 CellPath, UK) and stored at -80 °C. Samples were sectioned using a Cryostat (CM 1850, Leica
808 Biosystems, Germany) and 8µm thick sections were collected using Kawamoto's film method.⁴
809 Stainings (Goldner's Trichrome and Von Kossa) were subsequently carried out on the cryotape.
810 Sections were mounted using Super Cryomounting Medium (SCMM) type R3 (Section LAB, Co.
811 Ltd. Japan) and UV cured for 30 min to photo-polymerise the SCMM. Slides were imaged the
812 following day using a Zeiss Axiovert 200 (Carl Zeiss, Germany).

813

814

815 **Supplementary Information**

816 The Supporting Information contains detailed explanation of the experimental methods and
817 additional figures.

820 **Acknowledgements**

821 The work was supported by the ERC Starting Grant (STROFUNSCAFF), the Medical Research
822 Council (UK Regenerative Medicine Platform Acellular/Smart Materials-3D Architecture,
823 MR/R015651/1 to AM, JID and RO), and the AO Foundation (AOCMF-17-19M). The experiment
824 at the ISIS Neutron and Muon Source was allocated beam time under experiment number 1810221
825 (DOI:10.5286/ISIS.E.90604998) and collected on LARMOR. This work benefitted from the
826 SasView software, originally developed by the DANSE project under NSF award DMR-0520547.
827 BOO was supported by the Henry Royce Institute for Advanced Materials, funded through EPSRC
828 grants EP/R00661X/1, EP/S019367/1, EP/P025021/1 and EP/P025498/1. DJA thanks EPSRC for
829 an award of a fellowship (EP/L021978/2). We thank Dr Vicente Araullo-Peters and Dr Giulia
830 Mastroianni at Nanovision and School of Biological and Chemical Sciences (SBCS), QMUL as
831 well as Dr Janos Kanczler, Bone and Joint Research Group, Southampton for technical support.
832 We thank Dr Sarah Rogers and Dr Adam Washington from ISIS for SANS experiment. We thank
833 Dr Matthew Smith at Henry Royce Institute, Manchester for HRTEM and EDX analyses. We
834 thank Dr Richard Thorogate at London Centre for Nanotechnology for AFM analyses.

837 **Declaration of competing interest**

838 The authors declare that they have no known competing financial interests or personal
839 relationships that could have appeared to influence the work reported in this paper.

842 **References**

- 843 1. Wegst, U. G. K.; Bai, H.; Saiz, E.; Tomsia, A. P.; Ritchie, R. O. Bioinspired structural
844 materials. *Nat. Mater.* **2015**, 14, 23-36.
- 845 2. Elsharkawy, S.; Mata, A. Hierarchical biomineralization: from nature's designs to synthetic

- materials for regenerative medicine and dentistry. *Adv. Healthc. Mater.* **2018**, *7*, 1800178.
3. Asenath-Smith, E.; Li, H.; Keene, E. C.; She, Z. W.; Estroff, L. A. Crystal growth of calcium carbonate in hydrogels as a model of biomineralization. *Adv. Funct. Mater.* **2012**, *22*, 2891-2914.
4. Lemloh, M.-L.; Altintoprak, K.; Wege, C.; Weiss, I. M.; Rothenstein, D. Biogenic and synthetic peptides with oppositely charged amino acids as binding sites for mineralization. *Materials*, **2017**, *10*, 119.
5. Pohnert, G. Biomineralization in diatoms mediated through peptide- and polyamine-assisted condensation of silica. *Angew. Chem. Int. Ed.* **2002**, *41*, 3167-3169.
6. Evans, J. S. Composite materials design: biomineralization proteins and the guided assembly and organization of biomineral nanoparticles. *Materials* **2019**, *12*, 581.
7. Pigliacelli, C.; Sánchez-Fernández, R.; García, M. D.; Peinador, C.; Pazos, E. Self-assembled peptide–inorganic nanoparticle superstructures: from component design to applications. *Chem. Commun.* **2020**, *56*, 8000-8014.
8. Okesola, B. O.; Suravaram, S. K.; Parkin, A.; Smith, D. K. Selective extraction and *in situ* reduction of precious metal salts from model waste to generate hybrid gels with embedded electrocatalytic nanoparticles. *Angew. Chem. Int. Ed.* **2016**, *55*, 183-187.
9. Xavier, J. R.; Thakur, T.; Desai, P.; Jaiswal, M. K.; Sears, N.; Cosgriff-Hernandez, E.; Kaunas, R.; Gaharwar, A. K. Bioactive nanoengineered hydrogels for bone tissue engineering: a growth-factor-free approach. *ACS Nano*, **2015**, *9*, 3109-3118.
10. Elsharkawy, S.; Al-Jawad, M.; Pantano, M. F.; Tejeda-Montes, E.; Mehta, K.; Jamal, H.; Agarwal, S.; Shuturminska, K.; Rice, A.; Tarakina, N. V.; Wilson, R. M.; Bushby, A. J.; Alonso, M.; Rodriguez-Cabello, J. C.; Barbieri, E.; Del Río Hernández, A.; Stevens, M. M.; Pugno, N. M.; Anderson, P.; A. Mata. Protein disorder–order interplay to guide the growth of hierarchical mineralized structures. *Nat. Commun.* **2018**, *9*, 2145.
11. Kim, E.; Agarwal, S.; Kim, N.; Hage, F. S.; Leonardo, V.; Gelmi, A.; Stevens, M. M. Bioinspired fabrication of DNA–Inorganic hybrid composites using synthetic DNA. *ACS Nano*, **2019**, *13*, 2888-2900.
12. Okesola, B. O.; Ni, S.; Derkus, B.; Galeano, C. C.; Hasan, A.; Wu, Y.; Ramis, J.; Buttery, L.; Dawson, J. I.; D'Este, M.; Oreffo, R. O. C.; Eglin, D.; Sun, H.; Mata, A. Growth-factor free multicomponent nanocomposite hydrogels that stimulate bone formation. *Adv. Funct.*

- 877 *Mater.* **2020**, 30, 1906205.
- 878 13. Slavik, P.; Smith, D. K. Hybrid hydrogels loaded with palladium nanoparticles – Catalysts
879 for environmentally-friendly Sonogashira and Heck cross-coupling reactions.
880 *Tetrahedron*, **2020**, 76, 131344.
- 881 14. Sugawara-Narutaki, A. Bio-inspired synthesis of polymer–inorganic nanocomposite
882 materials in mild aqueous systems. *Polym. J.* **2013**, 45, 269-276.
- 883 15. Saveleva, M. S.; Eftekhari, K.; Abalymov, A.; Douglas, T. E. L.; Volodkin, D.;
884 Parakhonskiy, B. V.; Skirtach, A. G. Hierarchy of hybrid materials—the place of
885 inorganics-in-organics in it, their composition and applications. *Front. Chem.* **2019**, 7.
- 886 16. Kim, Y.-Y.; Ganesan, K.; Yang, P.; Kulak, A. N.; Borukhin, S.; Pechook, S.; Ribeiro, L.;
887 Kröger, R.; Eichhorn, S. J.; Armes, S. P.; Pokroy, B.; Meldrum, F. C. An artificial
888 biomineral formed by incorporation of copolymer micelles in calcite crystals. *Nat. Mater.*
889 **2011**, 10, 890-896.
- 890 17. Mann, S. Self-assembly and transformation of hybrid nano-objects and nanostructures
891 under equilibrium and non-equilibrium conditions. *Nat. Mater.* **2009**, 8, 781-792.
- 892 18. Sadasivan, S.; Dujardin, E.; Li, M.; Johnson, C. J.; Mann, S. DNA-driven assembly of
893 mesoporous silica/gold satellite nanostructures. *Small* **2005**, 1, 103-106.
- 894 19. Nikitin, M. P.; Zdobnova, T. A.; Lukash, S. V.; Stremovskiy, O. A.; Deyev, S. M. Protein-
895 assisted self-assembly of multifunctional nanoparticles. *PNAS*. **2010**, 107, 5827.
- 896 20. Chan, M. S.; R. Landig; Choi, J.; Zhou, H.; Liao, X.; Lukin, M. D.; Park, H.; Lo, P. K.
897 Stepwise ligand-induced self-assembly for facile fabrication of nanodiamond-gold
898 nanoparticle dimers via noncovalent biotin-streptavidin interactions. *Nano Lett.* **2019**, 19,
899 2020-2026.
- 900 21. Xiang, X.-F.; Li, P.-J.; Liu, B.-F.; Tuning the superhydrophobic properties of hierarchical
901 nano-microstructural silica biomorph arrays grown at triphasic interfaces. *Sci. Rep.* **2020**,
902 10, 4596.
- 903 22. Campbell, C. J.; Klajn, R.; Fialkowski, M.; Grzybowski, B. A. One-step multilevel
904 microfabrication by reaction–diffusion. *Langmuir* **2005**, 21, 418-423.
- 905 23. Smoukov, S. K.; Bishop, K. J. M.; Klajn, R.; Campbell, C. J.; Grzybowski, B. A. Cutting
906 into solids with micropatterned gels. *Adv. Mater.* **2005**, 17, 1361-1365.
- 907 24. Smoukov, S. K.; Grzybowski, B. A. Maskless microetching of transparent conductive

- oxides (ITO and ZnO) and semiconductors (GaAs) based on reaction-diffusion. *Chem. Mater.* **2006**, 18, 4722-4723.
25. Lovrak, M.; Hendriksen, W. E. J.; Maity, C.; Mytnyk, S.; van Steijn, V.; Eelkema, R.; van Esch, J. H. Free-standing supramolecular hydrogel objects by reaction-diffusion. *Nat. Commun.* **2017**, 8, 15317.
26. Kurylo, I.; Gines, G.; Rondelez, Y.; Coffinier, Y.; Vlandas, A. Spatiotemporal control of DNA-based chemical reaction network via electrochemical activation in microfluidics. *Sci. Rep.* **2018**, 8, 6396.
27. Luo, H.; Leprince-Wang, Y.; Jing, G. Tunable growth of ZnO nanostructures on the inner wall of capillary tubes. *J. Phys. Chem. C* **2019**, 123, 7408-7415.
28. Campbell, C. J.; Smoukov, S. K.; Bishop, K. J. M.; Baker, E.; Grzybowski, B. A. Direct printing of 3D and curvilinear micrometer-sized architectures into solid substrates with sub-micrometer resolution. *Adv. Mater.* **2006**, 18, 2004-2008.
29. Kleiman, M.; Brubaker, K. S.; Nguyen, D. T.; Esser-Kahn, A. P. Bio-inspired morphogenesis using microvascular networks and reaction-diffusion. *Chem. Mater.* **2015**, 27, 4871-4876.
30. Nakouzi, E.; Steinbock, O. Self-organization in precipitation reactions far from the equilibrium. *Sci. Adv.* **2016**, 2, e1601144.
31. Okesola, B. O.; Mata, A. Multicomponent self-assembly as a tool to harness new properties from peptides and proteins in material design. *Chem. Soc. Rev.* **2018**, 47, 3721-3736.
32. Gaharwar, A. K.; Cross, L. M.; Peak, C. W.; Gold, K.; Carrow, J. K.; Brokesh, A.; Singh, K. A. 2D Nanoclay for Biomedical Applications: Regenerative Medicine, Therapeutic Delivery, and Additive Manufacturing. *Adv. Mater.* **2019**, 31, 1900332.
33. Mousa, M.; Evan, N. D.; Oreffo, R. O. C.; Dawson, J. I. Clay nanoparticles for regenerative medicine and biomaterial design: A review of clay bioactivity. *Biomaterials* **2018**, 159, 204-214.
34. Gaharwar, A. K.; Mukundan, S.; Karaca, E.; Dolatshahi-Pirouz, A.; Patel, A.; Rangarajan, K.; Mihaila, S. M.; Iviglia, G.; Zhang, H.; Khademhosseini, A. Nanoclay-enriched poly(ϵ -caprolactone) electrospun scaffolds for osteogenic differentiation of human mesenchymal stem cells. *Tissue Eng. Part A*, **2014**, 20, 2088-2101.
35. Kerativitayanan, P.; Gaharwar, A. K. Elastomeric and mechanically stiff nanocomposites

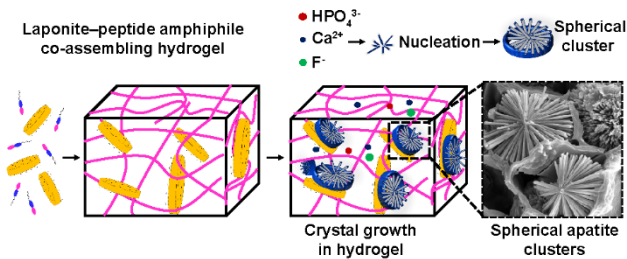
- from poly(glycerol sebacate) and bioactive nanosilicates. *Acta Biomater.* **2015**, 26, 34-44.
36. Nojoomi, A.; Tamjid, E.; Simchi, A.; Bonakdar, S.; Stroeve, P. Injectable polyethylene glycol-laponite composite hydrogels as articular cartilage scaffolds with superior mechanical and rheological properties. *Int. J. Polym. Mater.* **2017**, 66, 105-114.
37. Basu, S.; Pacelli, S.; Feng, Y.; Lu, Q; Wang, J.; Paul, A. Harnessing the noncovalent interactions of dna backbone with 2d silicate nanodisks to fabricate injectable therapeutic hydrogels. *ACS Nano* **2018**, 12, 9866-9880.
38. Su, D.; Jiang, L.; Chen, X.; Dong, J.; Shao, Z. Enhancing the gelation and bioactivity of injectable silk fibroin hydrogel with laponite nanoplatelets. *ACS Appl. Mater. Interfaces* **2016**, 8, 9619-9628.
39. Liu, B.; Li, J.; Lei, X.; Miao, S.; Zhang, S.; Cheng, P.; Song, Y.; Wu, H.; Gao, Y.; Bi, L.; Pei, G. Cell-loaded injectable gelatin/alginate/LAPONITE® nanocomposite hydrogel promotes bone healing in a critical-size rat calvarial defect model. *RSC Adv.* **2020**, 10, 25652 – 25661.
40. Koshy, S. T.; Zhang, D. K.Y.; Grolman, J. M.; Stafford, A. G.; Mooney, D. J; Injectable nanocomposite cryogels for versatile protein drug delivery. *Acta Biomater.* **2018**, 65, 36 – 43.
41. Page, D. J.; Clarkin, C. E.; Mani, R.; Khan, N. A.; Dawson, J. I.; Evans, N. D. Injectable nanoclay gels for angiogenesis. *Acta Biomater.* **2019**, 100, 378 – 387.
42. Capito, R. M.; Azevedo, H. S.; Velichko, Y. S.; Mata, A.; Stupp, S. I. Self-assembly of large and small molecules into hierarchically ordered sacs and membranes. *Science*, **2008**, 319, 1812.
43. Inostroza-Brito, K. E.; Collin, E.; Siton-Mendelson, O.; Smith, K. H.; Monge-Marcet, A.; Ferreira, D. S.; Rodríguez, R. P.; Alonso, M.; Rodríguez-Cabello, J. C.; Reis, R. L.; Sagués, F.; Botto, L.; Bitton, R.; Azevedo, H. S.; Mata A. Co-assembly, spatiotemporal control and morphogenesis of a hybrid protein–peptide system. *Nat. Chem.* **2015**, 7, 897-904.
44. Hedegaard, C. L.; Collin, E. C.; Redondo-Gómez, C.; Nguyen, L. T. H.; Ng, K. W.; Castrejón-Pita, A. A.; Castrejón-Pita, J. R.; Mata, A. Hydrodynamically guided hierarchical self-assembly of peptide–protein bioinks. *Adv. Funct. Mater.* **2018**, 28, 1703716.
45. Okesola, B. O.; Lau, H. K.; Derkus, B.; Boccorh, D. K.; Wu, Y.; Wark, A. W.; Kiick, K.

- 1
2
3 970 L.; Mata, A. Covalent co-assembly between resilin-like polypeptide and peptide
4 971 amphiphile into hydrogels with controlled nanostructure and improved mechanical
5 972 properties. *Biomater. Sci.* **2020**, 8, 846-857.
6
7
8 973 46. Okesola, B. O.; Wu, Y.; Derkus, B.; Gani, S.; Wu, D.; Knani, D. Smith, D. K.; Adams, D.
9 974 J.; Mata, A. Supramolecular self-assembly to control structural and biological properties
10 975 of multicomponent hydrogels. *Chem. Mater.* **2019**, 31, 7883-7897.
11
12
13 976 47. Zechel, S.; Hager, D. M.; Priemel, T.; Harrington, J. M. Healing through histidine:
14 977 bioinspired pathways to self-healing polymers via imidazole-metal coordination.
15 978 *Biomimetics* **2019**, 4, 20.
16
17
18 979 48. Wang, Q.; Mynar, J. L.; Yoshida, M.; Lee, E.; Lee, M.; Okuro, K.; Kinbara, K.; T. Aida,
19 980 High-water-content mouldable hydrogels by mixing clay and a dendritic molecular binder.
20 981 *Nature*, **2010**, 463, 339-343.
21
22
23 982 49. Mata, A.; Palmer, L.; Tejeda-Montes, E.; Stupp, S. I. in *Nanotechnology in Regenerative*
24 983 *Medicine: Methods and Protocols*, eds. M. Navarro and J. A. Planell, Humana Press,
25 984 Totowa, NJ, 2012, pp. 39-49.
26
27
28 985 50. Shi, J.; Wang, C.; Ngai, T.; Lin, W. Diffusion and binding of laponite clay nanoparticles
29 986 into collagen fibers for the formation of leather matrix. *Langmuir* **2018**, 34, 7379-7385.
30
31
32 987 51. [https://www.3ds.com/products-services/biovia/products/molecular-modeling-](https://www.3ds.com/products-services/biovia/products/molecular-modeling-simulation/biovia-materials-studio/)
33 988 [simulation/biovia-materials-studio/](https://www.3ds.com/products-services/biovia/products/molecular-modeling-simulation/biovia-materials-studio/), 2020.
34
35
36 989 52. Appel, E. A.; Tibbitt, M. W.; Webber, M. J.; Mattix, B. A.; Veis, O.; Langer, R. Self-
37 990 assembled hydrogels utilizing polymer-nanoparticle interactions. *Nat. Commun.* **2015**, 6,
38 991 6295.
39
40
41 992 53. Ligorio, C.; Zhou, M.; Wychowaniec, J. K.; Zhu, X.; Bartlam, C.; Miller, A. F.;
42 993 Vijayaraghavan, A.; Hoyland, J. A.; Saiani, A. Graphene oxide containing self-assembling
43 994 peptide hybrid hydrogels as a potential 3D injectable cell delivery platform for
44 995 intervertebral disc repair applications. *Acta Biomater.* **2019**, 92, 92-103.
45
46
47 996 54. Brown, N.; Lei, J.; Zhan, C.; Shimon, L. J. W.; Adler-Abramovich, L.; Wei, G.; Gazit, E.
48 997 Structural polymorphism in a self-assembled tri-aromatic peptide system. *ACS Nano*, **2018**,
49 998 12, 3253-3262.
50
51
52 999 55. Ren, Y.; Ma, Z.; Morris, R. E.; Liu, Z.; Jiao, F.; Dai, S.; Bruce, P. G. A solid with a
53 1000 hierarchical tetramodal micro-meso-macro pore size distribution. *Nat. Commun.* **2013**, 4,
54
55
56
57
58
59
60

1
2
3 1001 2015.
4
5 1002 56. Ng, K. C.; Burhan, M.; Shahzad, M. W.; Ismail, A. B. A universal isotherm model to
6
7 1003 capture adsorption uptake and energy distribution of porous heterogeneous surface. *Sci.*
8
9 1004 *Rep.* **2017**, 7, 10634.
10 1005 57. Cao, Y.; Mei, M. L.; Li, Q.-L.; Lo, E. C. M.; Chu, C. H. Polydopamine-induced tooth
11
12 1006 remineralization. *ACS Appl. Mater. Interfaces*, **2014**, 6, 410-420.
13
14 1007 58. Habraken, W. J. E. M.; Tao, J.; Brylka, L. J.; Friedrich, H.; Bertinetti, L.; Schenk, A. S.;
15
16 1008 Verch, A.; Dmitrovic, V.; Bomans, P. H. H.; Frederik, P. M.; Laven, J.; van der Schoot,
17
18 1009 P.; Aichmayer, B.; de With, G.; DeYoreo, J. J.; Sommerdijk, N. A. J. M. Ion-association
19
20 1010 complexes unite classical and non-classical theories for the biomimetic nucleation of
21
22 1011 calcium phosphate. *Nat. Commun.* **2013**, 4, 1507.
23
24 1012 59. Mann, S. The chemistry of form. *Angew. Chem. Int. Ed.*, **2000**, 39, 3392-3406.
25
26 1013 60. De Yoreo, J. J.; Gilbert, P. U. P. A.; Sommerdijk, N. A. J. M.; Penn, R. L.; Whitlam, S.
27
28 1014 Joester, D.; Zhang, H.; Rimer, J. D.; Navrotsky, A.; Banfield, J. F.; Wallace, A. F.; Michel,
29
30 1015 F. M.; Meldrum, F. C.; Cölfen, H.; Dove, P. M. Crystallization by particle attachment in
31
32 1016 synthetic, biogenic, and geologic environments. *Science*, **2015**, 349, aaa6760.
33
34 1017 61. Kumar, M.; Luo, H.; Román-Leshkov, Y.; Rimer, J. D. SSZ-13 crystallization by particle
35
36 1018 attachment and deterministic pathways to crystal size control. *J. Am. Chem. Soc.*, **2015**,
37
38 1019 137, 13007-13017.
39
40 1020 62. Asenath-Smith, E.; Hovden, R.; Kourkoutis, L. F.; L. A. Estroff, L. A. Hierarchically
41
42 1021 structured hematite architectures achieved by growth in a silica hydrogel. *J. Am. Chem.*
43
44 1022 *Soc.* **2015**, 137, 5184-5192.
45
46 1023 63. Seto, J.; Ma, Y.; Davis, S. A.; Meldrum, F.; Gourrier, A.; Kim, Y.-Y.; Schilde, U.; M.
47
48 1024 Sztucki, M.; Burghammer, M.; Maltsev, S.; Jäger, C.; Cölfen, H. Structure-property
49
50 1025 relationships of a biological mesocrystal in the adult sea urchin spine. *PNAS*, 2012, **109**,
51
52 1026 3699.
53
54 1027 64. Sargeant, T. D.; Aparicio, C.; Goldberger, J. E.; Cui, H; Stupp, S. I. Mineralization of
55
56 1028 peptide amphiphiles nanofibers and its effect on differentiation of human mesenchymal
57
58 1029 stem cells. *Acta biomater.* **2012**, 8, 2456-2465.
59
60 1030 65. Liu, Y.; Meng, H.; Konst, S.; Sarmiento, R.; Rajachar, R.; Lee, B. P. injectable dopamine-
1031
modified poly(ethylene glycol) nanocomposite hydrogel with enhanced adhesive property

- and bioactivity. *ACS Appl. Mater. Interfaces*, **2014**, 6, 16982-16992.
66. de Aza, P. N.; Santos, C.; Pazo, A.; de Aza, S.; Cuscó, R.; Artús, L. Vibrational properties of calcium phosphate compounds. 1. raman spectrum of β -tricalcium phosphate. *Chem. Mater.* **1997**, 9, 912-915.
67. Kurouski, D.; Van Duynea, R. P.; Lednev, I. K. Exploring the structure and formation mechanism of amyloid fibrils by Raman spectroscopy: a review. *Analyst*, **2015**, 140, 4967 – 4980.
68. Nakayama, M.; Kajiyama, S.; Kumamoto, A.; Nishimura, T.; Ikuhara, Y.; Yamato, M.; Kato, T. Stimuli-responsive hydroxyapatite liquid crystal with macroscopically controllable ordering and magneto-optical functions. *Nat. Commun.* **2018**, 9, 568.
69. Marshall, K. M.; Kanczler, J. M.; Oreffo, R. O. C. J. Evolving applications of the egg: chorioallantoic membrane assay and *ex vivo* organotypic culture of materials for bone tissue engineering. *Tissue Eng.*, **2020**, 11, 1 – 25.

1
2
3 1059 Graphic for Table of Content
4



1060
1061
1062